Exploration for multiferroics in hexaferrites

YUJI HIRAOKA

MARCH 2013

Exploration for multiferroics in hexaferrites

A dissertation submitted to
THE GRADUATE SCHOOL OF ENGINEERING SCIENCE
OSAKA UNIVERSITY
in partial fulfillment of the requirements for the degree of
DOCTOR OF PHILOSOPHY IN ENGINEERING

BY

YUJI HIRAOKA

MARCH 2013

Abstract

Multiferroics, i.e., materials that show both magnetic and ferroelectric orders simultaneously, have been attracting renewed interest and have been extensively studied in terms of both fundamental and technological points of view in the past decade. A class of multiferroics known as "spiral-induced ferroelectrics" often shows a giant magneto-electric effect, i.e., the phenomenon of inducing magnetic (electric) polarization by applying an external electric (magnetic) field, due to the fact that the origin of their ferroelectricity is driven by spiral magnetism which sensitively responds to an applied magnetic field. Thus, it is expected that this type of multiferroics will allow new types of device applications by using the magneto-electric effect, such as memory devices in which magnetic and/or ferroelectric domains are controlled by electric and/or magnetic fields.

However, until recently, the working temperature of this type of multiferroics had been low, typically below 40 K, which hampered the application. In 2005 the discovery of a spiral-induced ferroelectricity up to ~ 130 K in a Y-type hexaferrite, $Ba_{0.5}Sr_{1.5}Zn_2Fe_{12}O_{22}$ [ZnY(1.5)] changed the situation. Hexaferrites are composed of six main types [M-, X-, W-, Y-, Z-, and U- type], and it is reported that some of them show spiral magnetic structures above room temperature. Stimulated by the discovery of multiferroics in ZnY(1.5), many multiferroic hexaferrites have been discovered, and expected for multiferroic devices.

In this type of multiferroics, spin-chirality, i.e., right- or left-handedness of an ordered magnetic state, of the spiral magnetic structure decides the direction of the electric polarization. Therefore, the observation of spatial distribution of the spin-chirality, that is "spin-chiral domains", is indispensable for an actual application of the multiferroics.

In this thesis, we focused on single crystals of hexaferrites although polycrystalline samples are mainly studied in most hexaferrite from a technical standpoint. We explored new multiferroic hexaferrites, and elucidated the multiferroic properties by means of electric and magnetic measurements, and neutron diffraction technique. In addition, we observed the spin-chiral domain structures by means of resonant circularly polarized X-ray diffraction technique.

We revealed following things in the present study:

First, we discovered a new multiferroic Y-type hexaferrites $Ba_{2-x}Sr_xNi_2Fe_{12}O_{22}$ [NiY(x)], and examined the Sr concentration *x* dependence of multiferroic properties in NiY(x) for $0 \leq x \leq 1.5$. We found that NiY(1.5) shows the largest electric polarization. Using neutron diffraction technique, We uncovered that the origin of ferroelectricity in NiY(1.5) are derived from a spiral magnetic structure which is similar to that in another multiferroic hexaferrite $Ba_2Mg_2Fe_{12}O_{22}$.

Second, we tried to optimize the Na_2O-Fe_2O_3 and BaO-B_2O_3 flux conditions to grow Z-type hexaferrites $(Ba,Sr)_3Co_2Fe_{24}O_{41}$ showing spiral-induced ferroelectricity above room temperature. Another room temperature multiferroics U-type $Sr_4Co_2Fe_{36}O_{60}$ [SrCoU] are also obtained as a by-product. This is the first report for the single crystal growth of SrCoU.

Finally, we observed the spin-chiral domains in proper screw of ZnY(1.5) and NiY(1.5) by means of resonant circularly polarized X-ray diffraction technique. We found that the spin-chiral domains are robust below the Néel temperature in ZnY(1.5) and that ferrimagnetic and spiral magnetic phases coexist at around the transition temperature in NiY(1.5). In addition, we examined magneto-electric cooling effects to the spin-chiral domains in ZnY(1.5).

Contents

Chapter 1 Introduction

Multiferroics, i.e., materials that show both magnetic and ferroelectric orders simultaneously, have been attracting renewed interest and have been extensively studied fundamentally and technologically in the past decade[1,2]. A class of multiferroics known as "magnetically-induced ferroelectrics" often show giant magnetoelectric effects, that is, remarkable changes in electric polarization in response to a magnetic field due to the fact the origin of their ferroelectricity is driven by magnetism which responds to an applied magnetic field. Thus, it is expected that the magnetically-induced ferroelectrics will provide new applications by using the magnetoelectric effect, such as memory devices in which magnetic and/or ferroelectric domains are controlled by electric and/or magnetic fields.

A large number of new magnetically-induced ferroelectrics have been reported for the past decade since the discovery of "spiral magnetic structure"-induced ferroelectrics $TbMnO_3$[3]. In the "spiral magnetic structure" - induced ferroelectrics, the spin-chirality, i.e., right- or left-handedness of the ordered magnetic state, plays an important role. To date, however, there has been no practical application employing the magnetoelectric effect of the magnetically-induced ferroelectrics. This is partly because none of the existing magnetically-induced ferroelectrics have combined large and robust electric and magnetic polarizations above room temperature until quite recently. The situation has changed slightly by the discovery of room-temperature magnetoelectricity in a ferrite with a hexagonal structure, polycrystalline $Sr_3Co_2Fe_{24}O_{41}$, in 2010[4]. Thus, hexaferrites are promising candidate materials for multiferroic devices. In this chapter, we review multiferroics, magneto-electric (ME) effects, physical properties of hexagonal ferrites, including their crystal structure, magnetism, and resulting magnetoelectricity, and the resonant circularly polarized x-ray diffraction technique as a powerful tool to distinguish spin-chirality.

1.1. Multiferroics

Multiferroics are classified into several different types depending on the origins of their inversion symmetry breaking[1,2] [e.g., "$6s^2$ lone pair"[5], "geometric structural transition"[6], "charge ordering"[7,8,9], and "magnetic ordering" [10]]. Among these various multiferroics, extensive studies of ferroelectrics originating from magnetic orders, i.e., magnetically-induced ferroelectrics in which the inversion symmetry breaking and resultant ferroelectricity are induced by complex magnetic orders, were triggered almost a decade ago by the discovery of multiferroic nature in a perovskite-type rare-earth manganite $TbMnO_3$. Several kinds of magnetic structures which can break the inversion symmetry have been reported, e.g., a collinear "up-up-down-down" antiferromagnetic structure in Ca_3CoMnO_6[11], noncollinear "cycloidal spiral" magnetic structure in $TbMnO_3$ and "proper-screw" spiral structure in $CuFeO_2$[12].

Ferroelectricity induced by "cycloidal spiral" magnetic structures

In the mechanism of ferroelectricity of the hexaferrites, "cycloidal spiral" magnetic structure plays an important role. Katsura et al[13,14] first considered that spin current (or vector spin chirality: $\boldsymbol{S}i \times \boldsymbol{S}j$) induced between noncollinearly coupled spins leads to microscopic electric polarization Δp, known as the spin current model . Sergienko and Dagotto reported that the inverse Dzyaloshinskii – Moriya (DM) effect can cause the microscopic electric polarization ΔP though electron-lattice interaction when an oxygen ion is placed amid two noncollinearly coupled magnetic moments[15]. In either theorem, ΔP is written by

$$\boldsymbol{\Delta P} = A\boldsymbol{e}_{ij} \times (\boldsymbol{S}_i \times \boldsymbol{S}_j) \tag{1-1}$$

where A is a constant proportional to the spin-orbit coupling and superexchange interaction, and $\boldsymbol{e}_{ij}$ is the vector connecting two sites, i and j, along the propagation vector of a spiral structure [Figure 1.1 (a)]. As shown in Figure 1.1(b) and (c), microscopic electric polarization ΔP is to be uniform when the non-collinearly coupled magnetic moments are aligned in a cycloidal spiral manner. As a result, macroscopic electric polarization P appears in the rotation plane and perpendicular to the propagation vector of the spiral. The direction of P is decided by spiral-chirality, that is, counter clockwise (CCW) or clockwise (CW) to the cycloidal spiral components. In this type of multiferroics, magnetic order and ferroelectric order are deeply coupled, which enables us to control the magnetic and/or ferroelectric structure by perturbation of electric or magnetic fields.

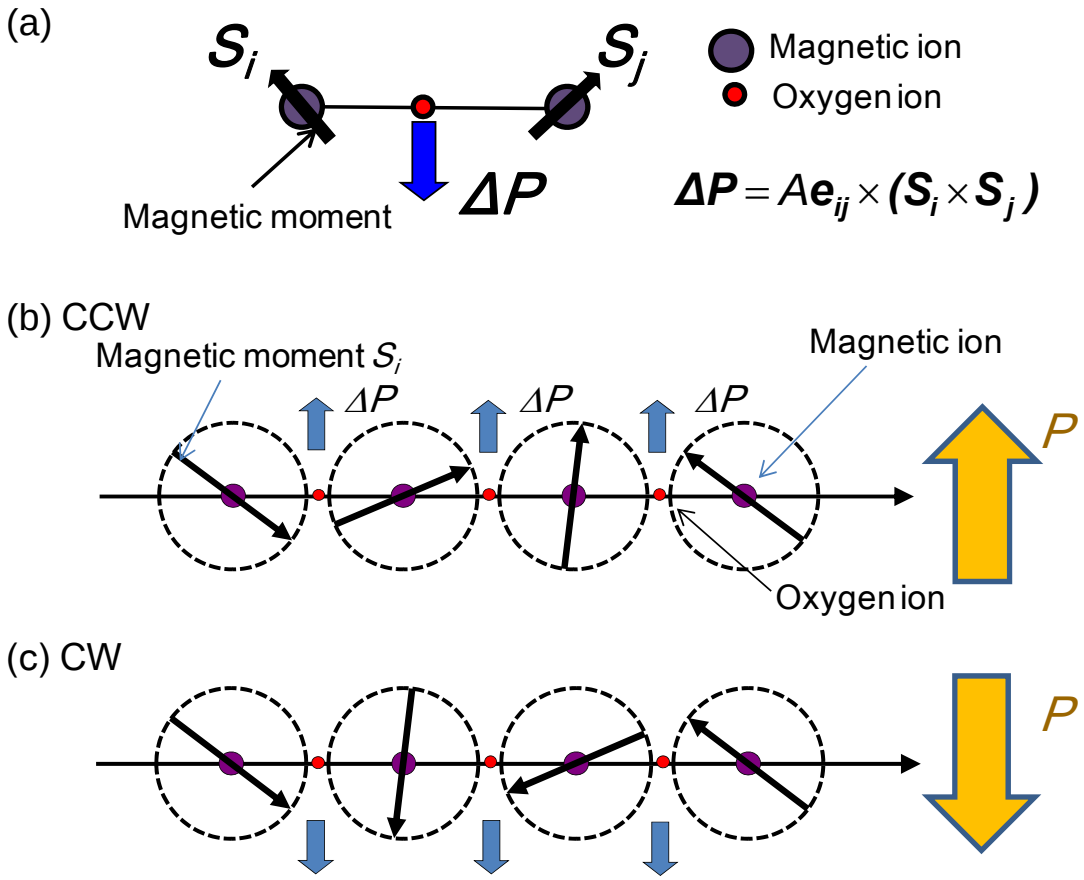

Figure 1.1 Schematic configuration of (a)the spin current model (or Inverse DM effect). Expected macroscopic electric polarization *P* in cycloidal spirals of (b) counter clockwise [CCW] and (c) clockwise [CW].

1.2. Magneto-electric (ME) effect

It was discovered by Faraday that there is a connection between electricity and magnetism, and the connection was then theoretically described by Maxwell. The magneto-electric (ME) effect, which is the induction of magnetization by an electric field or the induction of electric polarization by a magnetic field, was assumed by Pierre Curie on the basis of symmetry consideration in 1894[16]. The ME effect was actively studied in the 1960s and 1970s[17,18] after the theoretical prediction by Dzyaloshinskii using an oxide material Cr_2O_3 in 1959[19] and the first experimental observation by Astrov in 1960[20]. Since then, the effect has continued to attract interest.

Formulation of ME effect obtained from the expansion of the free energy

A systematic expression of contributions to the ME effect described in Landau theory can be

obtained from the expansion of the free energy F of a material[21] as follows:

$$F(\boldsymbol{E},\boldsymbol{H}) = F_0 - P_i^S E_i - M_i^S H_i - \frac{1}{2}\varepsilon_0\varepsilon_{ij}E_iE_j - \frac{1}{2}\mu_0\mu_{ij}H_iH_j - \alpha_{ij}E_iH_j - \frac{1}{2}\beta_{ijk}E_iH_jH_k - \frac{1}{2}\beta_{ijk}H_iE_jE_k - \cdots, \tag{1-2}$$

with E and H representing the electric and magnetic fields, respectively. Here, P_i^S, M_i^S, ε_0, μ_0, ε_{ij}, and μ_{ij} are spontaneous polarization, spontaneous magnetization, vacuum permittivity, vacuum permeability, relative permittivity, and relative permeability, respectively.

The differential leads to the electric polarization $\boldsymbol{P}$:

$$P_i(\boldsymbol{E},\boldsymbol{H}) = -\frac{\partial F}{\partial E_i}$$

$$= P_i^S + \varepsilon_0\varepsilon_{ij}E_j + \alpha_{ij}H_j + \frac{1}{2}\beta_{ijk}H_jH_k + \gamma_{ijk}H_iE_j - \cdots, \tag{1-3}$$

and to the magnetization $\boldsymbol{M}$:

$$M_i(\boldsymbol{E},\boldsymbol{H}) = -\frac{\partial F}{\partial H_i}$$

$$= M_i^S + \mu_0\mu_{ij}H_j + \alpha_{ij}E_i + \beta_{ijk}E_iH_j + \frac{1}{2}\gamma_{ijk}H_iE_j - \cdots \tag{1-4}$$

The tensors α_{ij} corresponds to the induction of $\boldsymbol{P}$($\boldsymbol{M}$) by H(E), which is designated as the linear ME effect:

$$P_i = \alpha_{ij}H_j \text{ and } M_j = \alpha_{ij}\ (\boldsymbol{P} = \tilde{\alpha}\boldsymbol{H} \text{ and } \boldsymbol{M} = \tilde{\alpha}\boldsymbol{E}), \tag{1.5}$$

where α_{ij} is the linear ME effect coefficient, which is a component of the linear ME tensor $\tilde{\alpha}$. The tensor $\tilde{\beta}$ and $\tilde{\gamma}$ are the coefficient for the higher order ME effect. In general, the value of $\tilde{\alpha}$ is widely used as evaluation of the ME effect. Therefore, large ME effect is expected. In magnetically-induced ferroelectrics, the electric polarization and magnetic order are coupled with, and therefore a large ME effect is expected. This type of multiferroics is known as "magneto-electric multiferroics".

1.3. Hexaferrites

Hexaferrites have been widely used in permanent magnets and absorbers of electromagnetic waves since the intensive studies by researchers in Philips Laboratories in 1950s. Hexaferrites are classified into main six types: M-type, W-type, X-type, Y-type, Z-type, and U-type (Details of their chemical formulas will be given in the next subsection.)[22]. The first report of a compound which

belongs to hexaferrites is published in the early twenty century. The compound was found in a magnetic mineral, called “magnetoplumbite” in 1925[23]. Its crystal structure was identified as a hexagonal structure with the composition of $PbFe_{7.5}Mn_{3.5}Al_{0.5}Ti_{0.5}O_{19}$[24]. After the discovery, a number of isomorphous compounds including $BaFe_{12}O_{19}$ were suggested, although their crystallographic structures were not investigated until after the Second World War. Then, Philips Laboratories led the way in developing ferrites under the direction of Snoek. $BaFe_{12}O_{19}$ consists of the same hexagonal structure with the magnetoplumbite [25] and is known by many names, such as barium ferrite, ferroxdure, M-type hexaferrite, and BaM. Following the studies on the M-type hexaferrite, W-type $BaFe_{18}O_{27}$, was grown and identified by Wijn[26] and Braun[27], respectively. Detailed reports of all the main hexaferrite phases were published by Philips Laboratories in the 1950s, culminating in Smit and Wijin’s excellent book “*Ferrites*”, published in 1959[28].

Crystallographic structures of hexaferrites

All hexaferrites have the same structural components and highly complex crystal structures, which can be interpreted in various ways. Here, we will introduce a commonly used way to describe the hexaferrite structures. Table 1.1 shows the structures of hexaferrites can be explained by stacking sequences of three basic blocks[Figure 1.2]: S [$Me_2Fe_4O_8$: spinel block], R [$BaFe_6O_{11}]^{2-}$, and T [$Ba_2Fe_8O_{14}$], where *Me* denotes divalent metal ions (e.g., Fe^{2+}, Co^{2+}, Ni^{2+}, Zn^{2+}, etc.)[28,29]. These blocks are composed of the stacking of two-dimensionally close-packed layers made by "large ions" Ba^{2+} and O^{2-}. Ba^{2+} can be substituted by Sr^{2+}, Pb^{2+}, and Ca^{2+} as discussed later. Fe^{3+} and Me^{2+} ions are set into the spaces surrounded by four and eight "large ions" and five oxygen ions, which are named tetragonal, octahedral, and bipyramid sites, respectively. As listed in Table 1.1, the hexaferrites are classified into six main types depending on their chemical formulas and stacking sequences: M-type [$BaFe_{12}O_{19}$], W-type [$BaMe_2Fe_{16}O_{27}$], Y-type [$Ba_2Me_2Fe_{12}O_{22}$], Z-type [$Ba_3Me_2Fe_{24}O_{41}$], X-type [$Ba_2Me_2Fe_{28}O_{46}$], and U-type [$Ba_4Me_2Fe_{36}O_{60}$]. Schematic crystal structures of these are illustrated in Figure 1.3. The most well-known hexaferrite is the M-type (magnetoplumbite) whose structure [Figure 1.3(a)] can be built up from the S blocks interposed by the R block and be symbolically describes as RSR*S*. (the * symbol means that the corresponding block has been turned 180° about the hexagonal *c* axis.) For the Y-type illustrated in Figure 1.3(c), the structure can be considered as an alternating stacking of the S and the T blocks along the *c* axis – TST'S'T"S" – , where the prime means the corresponding block is rotated 120° around this axis.

Type	Molecular formula	Hexaferrite blocks	*c* (Å)	Space group
M	$BaFe_{12}O_{19}$	RSR*S*	~23	$P6_3/mmc$
W	$BaMe_2Fe_{16}O_{27}$	RS_2R*S*_2	~33	$P6_3/mmc$
X	$Ba_2Me_2Fe_{28}O_{46}$	$(RSR*S*_2)_3$	~84	$R\text{-}3m$
Y	$Ba_2Me_2Fe_{12}O_{22}$	$(TS)_3$	~43	$R\text{-}3m$
Z	$Ba_3Me_2Fe_{24}O_{41}$	RSTSR*S*T*S*	~52	$P6_3/mmc$
U	$Ba_4Me_2Fe_{36}O_{60}$	$(RSR*S*TS*)_3$	~113	$R\text{-}3m$

$* = 180°$ rotation of that block around the *c*-axis

Table 1.1 Features of six main types of hexaferrites

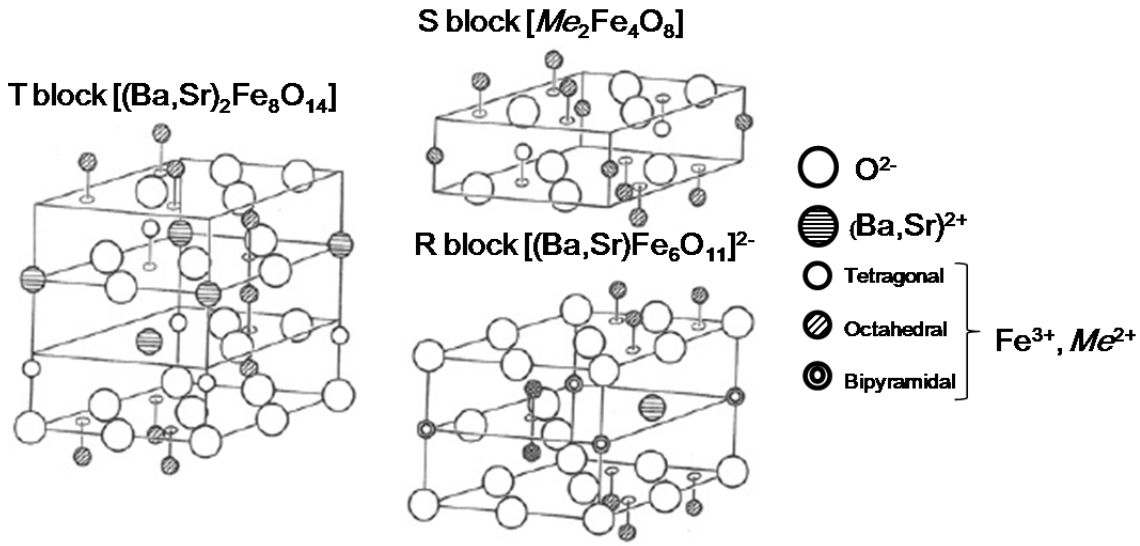

Figure 1.2 Three basic blocks: S [$Me_2Fe_4O_8$: spinel block], R [$BaFe_6O_{11}]^{2-}$, and T [$Ba_2Fe_8O_{14}$], where *Me* denotes a divalent metal ion (e.g., Fe^{2+}, Co^{2+}, Ni^{2+}, and Zn^{2+}) [29]

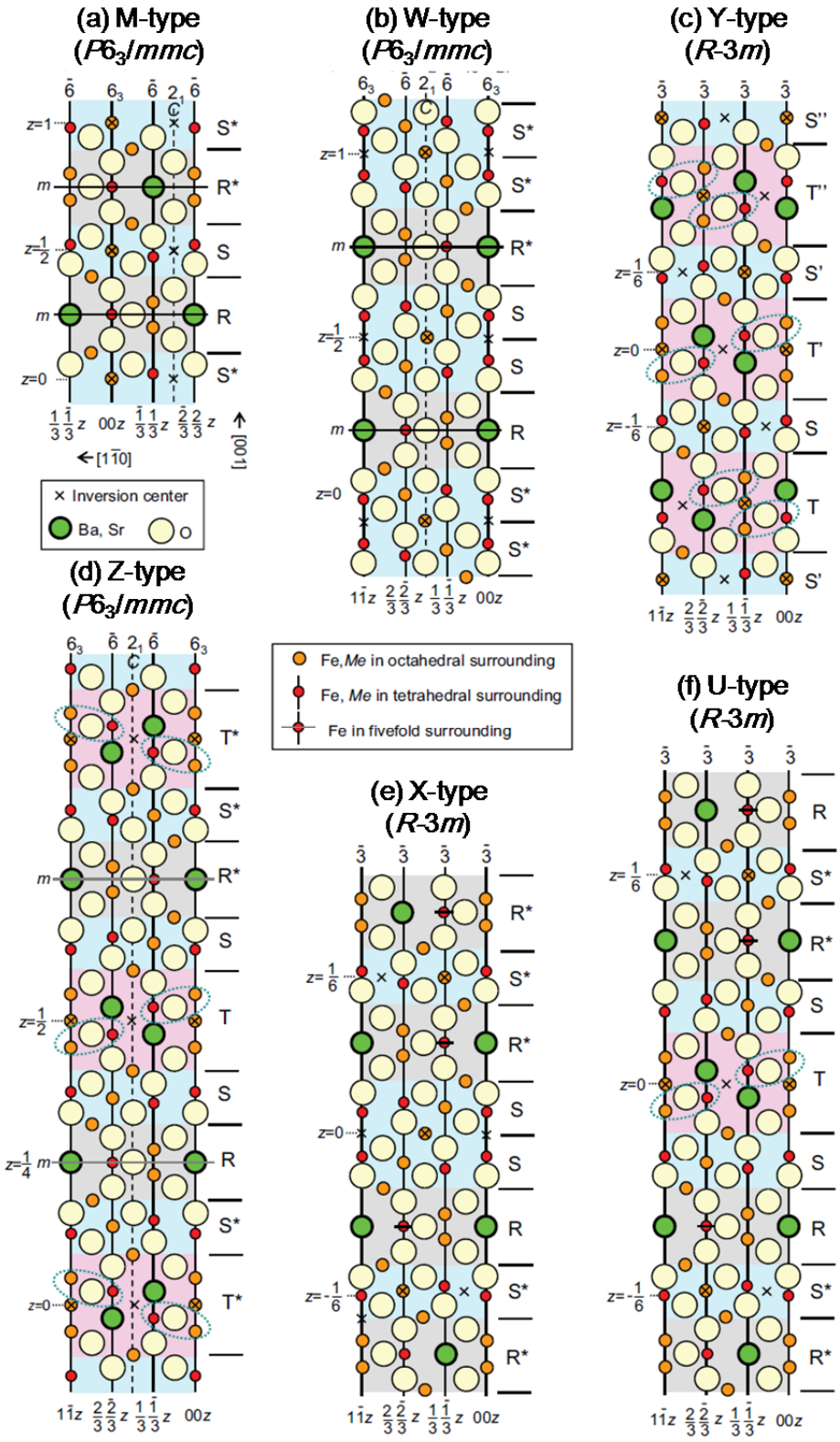

Figure 1.3 Schematic crystal structures of hexaferrites. The (110) cross section views of a (a) M-type (Ba,Sr)$Fe_{12}O_{19}$, (b) W-type (Ba,Sr)$Me_2Fe_{16}O_{27}$, (c) Y-type (Ba,Sr)$_2Me_{12}O_{22}$, (d)

Z-type (Ba,Sr)$_3$*Me*$_2$Fe$_{24}$O$_{41}$, (e) X-type (Ba,Sr)$_2$*Me*$_2$Fe$_{28}$O$_{46}$, (f)U-type (Ba,Sr)$_4$*Me*$_2$Fe$_{36}$O$_{60}$ with the *c* axis vertical. The (Fe,*Me*)-O-(Fe,*Me*) bond angles surrounded by dashed blue ellipsoids are strongly affected by the ratio of Sr to Ba[30].

Another aspect of hexaferrites is their large unit cells, especially long *c* lengths. It is known that there are about 60 types of hexaferrites with unit cells larger than those of the above-mentioned six main phases[31]. We can classify them into two systems in terms of another definition of structural blocks. Here, we will introduce the way to describe the structure of hexaferrites by using the S' (*Me*$_2$Fe$_4$O$_8$), M' (BaFe$_{12}$O$_{19}$), and Y' (Ba$_2$*Me*$_2$Fe$_{12}$O$_{22}$) blocks as summarized in Figure 1.4. S', M' , and Y' correspond to S, S+R ,and S+T, respectively.

The hexaferrite system can fall into "a limited *M'-S'* series [*M'$_n$S'*]" and "a prolific *M'–Y'* group [*M'$_p$Y'$_m$*]" [31]. The main six hexaferrites except for M-type can be considered as W-type [n = 1], X-type [n = 2], Y-type [p = 0, m = 1], Z-type [p = 1, m = 1], and U-type [p = 2, m = 1] (Table 1.2) (n, m, p are natural numbers). According to ref. 31, $n \leq 6$ for *M'$_n$S'* series, and $p \leq 4$ and $m \leq 33$ for *M'$_p$Y'$_m$* have been obtained so far. Hexaferrite *M'$_4$Y'$_{33}$*, Ba$_{70}$Zn$_{66}$Fe$_{44}$O$_{802}$, has the largest unit cell (47,000 Å^3) of any known inorganic material, containing over 4100 atoms.

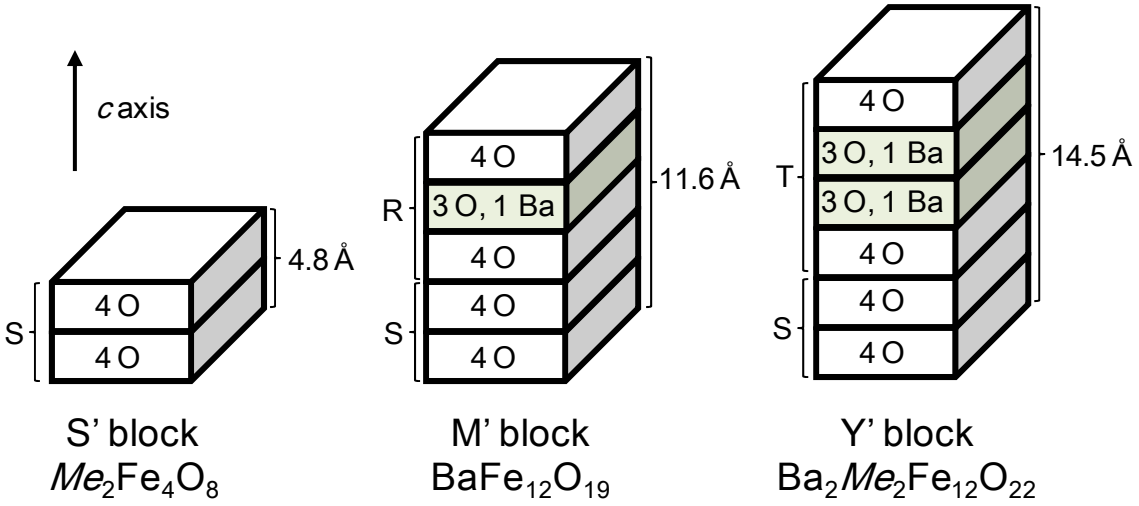

Figure 1.4 Schematic drawings of the three discrete building blocks that stack along the *c* axis to form numerous, ordered, mixed-layer hexaferrite structures; each block has the same cross-sectional dimensions and consists of individual layers with four oxygen atoms (4 O) or three oxygen atoms and one barium atom (3 O, 1Ba) [31]

Type	Molecular formula	Stacking sequence	Unit cell	c (Å)
M	$BaFe_{12}O_{19}$	M'	2 × M	~23
W	$BaMe_2Fe_{16}O_{27}$	$M'S'$	2 × W	~33
X	$Ba_2Me_2Fe_{28}O_{46}$	M'_2S'	3 × X	~84
Y	$Ba_2Me_2Fe_{12}O_{22}$	Y'	3 × Y	~43
Z	$Ba_3Me_2Fe_{24}O_{41}$	$M'Y'$	2 × Z	~52
U	$Ba_4Me_2Fe_{36}O_{60}$	M'_2Y'	3 × U	~113

Table 1.2 Descriptions of the molecular units of hexaferrites by means of M' and S' and Y' blocks.

Magnetic properties of hexaferrites

The basic magnetic structures of hexaferrites are collinearly-oriented ferrimagnetic structures, known as Gorter models[32] . However, it has been reported that some hexaferrites possess noncollinear magnetic ordered states including spiral magnetic structures, sometimes above room temperature, in such materials as M-type $Ba(FeSc)_{12}O_{19}$[33], W-type $BaNi_2Sc_2Fe_{14}O_{27}$[34] and Y-type $(Ba,Sr)_2Zn_2Fe_{12}O_{22}$ [35] , [36] and Z-type $(Ba,Sr)_3Zn_2Fe_{24}O_{41}$ [37] in earlier neutron diffraction measurements.

Multiferroic properties in hexaferrites

For many years, the weak points of multiferroics induced by spiral magnetic structures had been their low working temperatures. The situation changed with the discovery of intermediate phases in $Ba_{0.5}Sr_{1.5}Zn_2Fe_{12}O_{22}$ [hereafter ZnY(1.5)][38]. The magnetically-induced ferroelectricity of ZnY(1.5) was observed up to 130 K. Triggered by this research, many multiferroic hexaferrites have been discovered : M-type $Ba(Sc,Fe,Mg)_{12}O_{19}$ [39] , some of Y-type [see the next], Z-type $(Ba,Sr)_3Co_2Fe_{24}O_{41}4$[61] , and U-type $Sr_4Co_2Fe_{36}O_{60}$[40]. In the next, we introduce magnetic and magnetoelectric properties of Y-type hexaferrites, a well-known example. It is worth noting that "stable" spiral-induced ferroelectricity is observed in Y-, Z- and U-type, classified by the [$M'_pY'_m$] group, because spiral structures in M-type $Ba(Sc,Fe,Mg)_{12}O_{19}$ are easily destroyed by applying a magnetic field [39].

Multiferroic properties in Y-type hexaferrites – $Ba_{2-x}Sr_xMe_2Fe_{12}O_{22}$ [*Me*Y(x)]

Nearly all the Y-type hexaferrites have preferred their plane magnetization perpendicular to the *c*-axis at room temperature except *Me* = Co system in contrast with axial ferrimagnets M-type hexaferrites. The chemical formula of the Y-type hexaferrites is $Ba_{2-x}Sr_xMe_2Fe_{12}O_{22}$ [*Me*Y(x)], where *Me* is a small divalent cation [*Me* = Zn, Mg, Co, Ni, Cu, Fe etc.]. The first hexaferrite showing multiferroic properties is $Ba_{0.5}Sr_{1.5}Zn_2Fe_{12}O_{22}$ [ZnY(1.5)][38]. Followed by this discovery, ferroelectricity in other Y-type hexaferrites such as $(Ba,Sr)Zn_2(Fe,Al)_{12}O_{22}$[41,42], $Ba_2Mg_2Fe_{12}O_{22}$[43,44], $Ba_2(Mg,Zn)_2Fe_{12}O_{22}$[45], $(Ba,Sr)_2Ni_2Fe_{12}O_{22}$[46], $Ba_{0.3}Sr_{1.7}Co_2Fe_{12}O_{22}$[47], and $BaSrCoZnFe_{11}AlO_{22}$[48] have been reported. The multiferroicity of *Me* = Ni system will be discussed in the chapter 4.

In most of the multiferroic Y-type hexaferrites, proper screw or longitudinal conical magnetic structures play an important role in their multiferroic properties. A magnetic-structure model of ZnY(1.5), proposed in ref. 35, is commonly used to describe spiral magnetic structures. It interrupts the ferroelectric properties in most of magnetoelectric Y-type hexaferrites. Here, we will introduce the model in detail.

In this model, two kinds of structural blocks which are different from the T and S blocks mentioned above are assumed. One is an "L block" with large spin moments (μ_L), and the other is an "S block" having small spin moments (μ_S), as seen in Figure 1.5. Thus, the Y-type hexaferrite can be viewed as alternate stacks of L and S blocks along the hexagonal *c*-axis. Within the respective blocks, the magnetic moments on Fe (and *Me*) sites lying in the *ab*-plane are collinear and form a ferrimagnetic structure.

The boundary of these blocks is located between the 4th [Fe(4)] and 5th [Fe(5)] layers, as shown in Figure 1.5(a). In ZnY(1.5), the superexchange interaction across the boundary of these blocks, Fe(4)-O(2)-Fe(5) surrounded by blue dotted ellipses in Figure 1.5(a), is reinforced by replacing Ba with Sr, which is a key to the screw magnetic structure.

ZnY(1.5) shows the proper screw structure at the ground state [Figure 1.5 (b)], but transforms to a transverse conical [Figure 1.5 (c)] and the collinear ferromagnetically ordered state [Figure 1.5 (d)] by applying magnetic fields in the *ab*-plane. It is worth noting that the transverse conical one allows finite polarization by the spin current model although the proper screw structure does not allow it due to the fact ΔP in (1-1) should be zero.

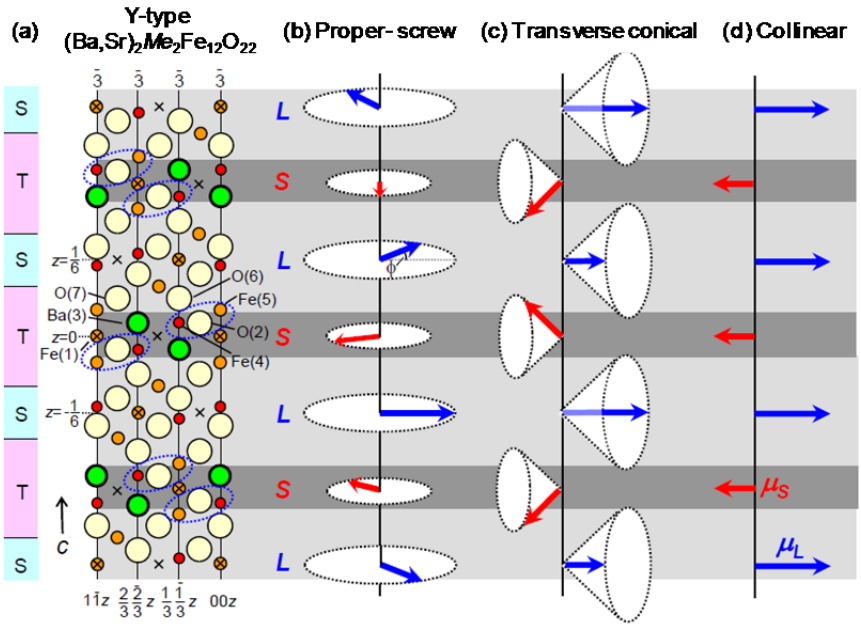

Figure 1.5 **Schematic (a) crystal and (b-d) proposed magnetic structures of magnetoelectric Y-type hexaferrites. In the Y-type hexaferrites, (b) the proper-screw (or longitudinal conical for MgY(0)) magnetic structure transforms into (c) the transverse conical one which allows finite polarization by applying a magnetic field along the c plane. By applying higher magnetic fields, (d) the collinear ferromagnetic ordered state appears. The long and short arrows indicate the effective moments of the L and S blocks, respectively[30].**

1.4. Resonant X-ray diffraction from magnetic materials

The extreme weakness of magnetic X-ray diffraction compared with non-magnetic scattering presents a considerable challenge to the experiments. By turning photon energy to the resonant levels of the magnetic ions, the weak magnetic diffraction can be enhanced by adding resonant scattering terms. With the development of the synchrotron radiation source and concomitant instruments, the observation of magnetic X-ray diffraction by means of resonant X-ray diffraction has been realized. One of the earliest studies of the screw magnetic structures is that for Holmium metal, which shows the proper screw below T_N = 133 K, by D. R. Harshman et al.[49]. They obtained a fifty fold resonant enhancement of a magnetic reflection by turning X-ray photon energy to Holmium L_3 absorption edges.

The theory of resonant X-ray diffraction from magnetic materials is well-described in a book by S. W. lovesey and S. P. Collins[50]. When the elastic resonant magnetic scattering length for a single atom can be written as the sum of three separate terms,

$$f_r^{E1}(E)=f_0(E)+f_{circ}(E)+f_{lin}(E)$$

where

$$\begin{cases} f_0(E) = -\left(\frac{3}{4\pi q}\right)(\boldsymbol{\varepsilon}'\cdot\boldsymbol{\varepsilon})\left[F^1_{+1}+F^1_{-1}\right] \\ f_{circ}(E) = -\mathrm{i}\left(\frac{3}{4\pi q}\right)(\boldsymbol{\varepsilon}'\times\boldsymbol{\varepsilon})\cdot\mathbf{m}\left[F^1_{-1}-F^1_{+1}\right] \\ f_{lin}(E) = -\left(\frac{3}{4\pi q}\right)(\boldsymbol{\varepsilon}'\cdot\mathbf{m})(\boldsymbol{\varepsilon}\cdot\mathbf{m})\left[2F^1_0-F^1_{+1}-F^1_{-1}\right] \end{cases} \quad (1\text{-}6)$$

and in terms of which the resonant cross-section is simply

$$\frac{\mathrm{d}\sigma}{\mathrm{d}\boldsymbol{\Omega}} = \left|f_r^{E1}(E)\right|^2 \quad (1\text{-}7)$$

In these expressions $E = \hbar qc$ is the photon energy, $\boldsymbol{\varepsilon}$ and $\boldsymbol{\varepsilon}'$ are the polarization vectors of the primary and secondary (scattered) beams, **m** represents the local moments direction, and $F^1{}_\nu$ are the strongly energy-dependent dimensionless resonant strengths for dipole transitions with a change in magnetic quantum number of ν. Only contributions from electric dipole transitions ($E1$) will be considered in our case.

The second and third terms in equations (1-6) include the local moments direction **m**, which plays an important role in resonant x-ray diffraction from magnetic materials.

1.5. Resonant circularly polarized X-ray diffraction from magnetic materials

In spiral-induced multiferroics, spin chirality of the spiral magnetic structure, i.e., right- or left-handedness of an ordered magnetic state (in section 1.1, counter clockwise or clockwise), plays an important role because it decides the direction of the electric polarization. Observation of the

spatial distribution of the spin-chirality, that is “spin-chiral domains”, is indispensable from a technical standpoint for an actual application of the multiferroics. However, observation of the spin-chiral domain structure is not as straight forward as that of conventional ferroic domains like the magnetic (ferroelectric) domains observed in ferromagnets (ferroelectrics).

To date, the spin-chiral domains have been observed mainly for rare earth metals (e.g., Tb and Ho) by only a few experimental techniques, such as diffraction topography using polarized neutrons[51,52] and scanning x-ray microdiffraction using resonant circularly polarized x rays [RcXRD] [53,54]. Whereas diffraction topography using polarized neutrons should reflect interior spin-chiral domain structures, scanning x-ray microdiffraction using RcXRD enables us to examine the spin-chiral domains on only the surface due to the short penetration depth of resonant x-ray.

Figure 1.6 (a) and (b) show a first example of the observation of the spin-chiral domains observed by scanning x-ray microdiffraction using RcXRD in the screw phase in Holmium metal. As we will discuss in equations (5-1) and (5-2) of chapter 5, intensities of magnetic diffraction by means of RcXRD with a helicity beam shows the dependence of the spin-chirality of the screw magnetic structure. Strong intensity regions in each figure correspond to either (c) right-handed or (d) left-handed chiral domains.

In the observation made by using the RcXRD, it is necessary to turn the energy of X-ray to a resonant level (L_{23} edges for the transition metals and rare earth metals) of the composing magnetic ions and use a highly-focused circular X-ray beam. In magnetic materials composed by the transition metal, including hexaferrites, the energy of L_{23} edges is in the soft x-ray region, where ultra-vacuum pressure is needed. These have hampered the observation of the spin-chiral domains using RcXRD. However, the recent development of synchrotron radiation and the accompanying instruments enable us to observe the spin-chiral domains.

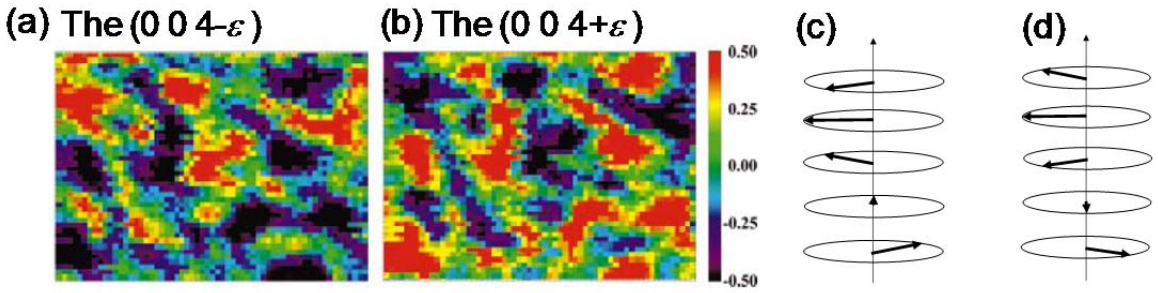

Figure 1.6 Observation of the spin-chiral domains of proper screw magnetic structure in Ho metal by scanning x-ray microdiffraction using RcXRD by (a) the (0 0 4-ε) magnetic reflection and (b)the (0 0 4+ε) magnetic reflection, respectively [normalized by sum of the (0 0 4+ε) and (0 0 4-ε) magnetic reflection intensities]. (c) and (d) are right- and left- handed screw, respectively[53].

1.6. Motivation of this work

Multiferroic hexaferrites are promising candidate materials for magneto-electric devices. We explored new multiferroic hexaferrites showing spiral magnetic structures, and elucidated the origin of the magneto-electric properties.

"Spin-chiral domain structure" in this type of multiferroics corresponds to the ferroelectric domain. The control of spin-chirality by means of external perturbations, e.g. magnetic and/or electric fields will attract renewed interest. Thus, we tried to examine and control spatial distributions of spin-chiral domains in two of the multiferroic hexaferrites, ZnY(1.5) and NiY(1.5) by scanning resonant x-ray microdiffraction .

In short, the goals of this thesis are as follows:

1. Discovery of a new multiferroic Y-type hexaferrites $Ba_{2-x}Sr_xNi_2Fe_{12}O_{22}$ [NiY(x)] and the elucidation of the origin of the magneto-electro effects in NiY(x).
2. Single crystal growth of multiferroic hexaferrites $(Ba,Sr)_3Co_2Fe_{24}O_{41}$ [(BaSr)CoZ].
3. Imaging for "spin-chiral domains" in multiferroic hexaferrites ZnY(1.5) and NiY(1.5).

We performed the experiments to achieve these goals.

Chapter 2 Experimental methods

2.1. Crystal growth of hexaferrites

To date, several methods for growing hexaferrite crystals have been reported[55,56]such as flux growth methods using Na_2O-Fe_2O_3 flux for M-, W-, X-, Y-, Z-, and U- type[57], and BaO-B_2O_3 flux for M- [58]and Y- type[59]. In this thesis work, we grew single crystals of several-types of hexaferrites by means of the Fe_2O_3-Na_2O flux and BaO-B_2O_3 flux. Experimental details of growth of the crystals will be shown in each chapter. Using a laboratory X-ray diffractometer, we checked the *d*-spacing perpendicular to the widest and highly-reflected face of the obtained crystals and identified the lattice constant *c* of each single crystal, and determined the type of the hexaferrites by utilizing each *c* axis length.

2.2. Measurements of magnetic and electric properties

For measurements of permittivity, electric polarization, and in-plane resistivity, the grown crystals were formed into thin plates (typically ~4×0.5×2 mm^3) with the widest faces including the *c* axis. Then, silver electrodes were deposited or made by pasting a silver paste onto the widest faces. The electric polarization *P* was obtained by integrating the current, which flowed while a magnetic field was swept, as a function of time. The permittivity was measured at 1 MHz or 100 kHz by an LCR meter (Agilent E4980A). The in-plane resistivity was measured by a two-probe method due to its high resistance. Lattice constants at room temperature were measured by using a four-circle X-ray diffractometer. Measurements of magnetization *M* were carried out by using commercial DC and superconducting quantum interference device (SQUID) magnetometers.

2.3. Neutron diffraction technique

Neutron diffraction measurements of a NiY(1.5) crystal were performed by using a triple-axis spectrometer PONTA installed at JRR-3, JAERI, Tokai, Japan. An incident neutron energy of 41 meV was adopted for all of the measurements. An external magnetic field *B* was applied parallel to the *b* axis with a split electromagnet. The sample was mounted with the *b* axis perpendicular to the scattering plane in a closed-cycle ^{4}He refrigerator.

2.4. Resonant circularly polarized X-ray diffraction technique [RcXRD]

Measurements of resonant X-ray magnetic diffraction of the cleaved surfaces of NiY(1.5) and

ZnY(1.5) were carried out using an ultra-high-vacuum diffractometer equipped at the beamline 17SU, SPring-8, Japan[60]. The features of the apparatus are listed in Table 2.1. The apparatus is shown in Figure 2.1, which enable us to achieve the ultra-high-vacuum (≤ 5×10^{-8} Pa). The ultra-high vacuum is indispensable when using the soft X-ray beam.

Energy range : 300 ~ 2000 eV
Highly-focused beam spot : ~30 μm× 15 μm
Ultrahigh-vacuum : 5×10^{-8} Pa
Polarization : π, σ, (+) helicity, (–) helicity
Sample manipulation : x, y, z, θ, 2θ, χ, ϕ
Temperature range : 30 ~ 300 K

Table 2.1 Features of the ultrahigh-vacuum diffractometer at the BL 17SU

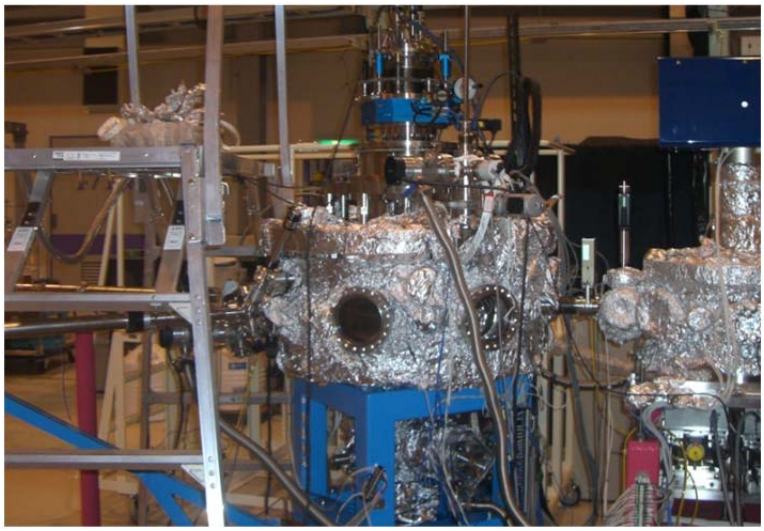

Figure 2.1 A picture of the ultrahigh-vacuum diffractometer at the BL 17SU

Figure 2.2 shows X-ray absorption spectra [XAS] of ZnY(1.5) at room temperature by measuring the flowing current in the sample with the energy of the incident photon changing. At 710 eV, where the XAS is maximum, an absorption by the Fe L_3 edge is observed. Turning the incident photon energy to the Fe L_3 edge (=710 eV), we performed experiments for ZnY(1.5) and NiY(1.5) crystals. The helicity of the incident beam was switched by the electromagnets of an undulator. The polarization of X-rays is defined by two orthogonal unit vectors $\boldsymbol{e}(1)$ and $\boldsymbol{e}(2)$ represented by σ and π, respectively, as illustrated in Figure 2.3. The scattering plane is spanned by vectors $\boldsymbol{k}_i$ and $\boldsymbol{k}_f$, which are the propagation vectors of the incident and diffracted beams, respectively. Vectors $\boldsymbol{k}$, $\boldsymbol{e}(1)$, and $\boldsymbol{e}(2)$ have the right-handed relation $\boldsymbol{k}/|\boldsymbol{k}| = \boldsymbol{e}(1) \times \boldsymbol{e}(2)$. Here, we denote the vectors of the right- and left-handed circular polarization by $\boldsymbol{e}(+)$ and $\boldsymbol{e}(-)$, respectively, and define the helicity as

positive and negative, respectively, as well:

$$\boldsymbol{e}^{(\pm)} = \mp\frac{i}{\sqrt{2}}(\boldsymbol{e}^{(1)} + i\boldsymbol{e}^{(2)}). \tag{2-1}$$

The circular polarization is expressed by a sum of $\boldsymbol{e}^{(1)}$ and $\boldsymbol{e}^{(2)}$ linear polarization, and the + (−) helicity beam that has the $\boldsymbol{e}^{(1)}$ component is advanced (behind) in time by a phase $\pi/2$ to the $\boldsymbol{e}^{(2)}$ component at the fixed position with the expression of the phase factor exp i ($\boldsymbol{k} \cdot \boldsymbol{r} - \omega t$) for an electromagnetic plane wave. In other words, when the observer is looking toward the beam source, the electric field of the + (−) helicity beam is counterclockwise (clockwise) in time [Figure 2.3] and has a left- (right-) handed screw-in space. Many textbooks for crystallography conventionally use the opposite sign for the phase factor, whereas our definition of handedness is opposite to that of optics. The crystals were mounted with the *c* axis in the scattering plane, as illustrated in Figure 2.3. For the imaging, the crystals were positioned with an *XYZ* translation stage with a 25-μm step, and the diffracted intensity of the (0 0 3–ε) magnetic reflection was measured at each point using a Si-photodiode sensor. (As depicted in Figure 2.3, the *X* direction is aligned along the *c* axis and in the *Z* direction is perpendicular to the scattering plane.) We focused the incident beam using Kirkpatrick-Baez configuration mirrors equipped just before the diffractometer. The spot size was ~30 μm horizontally and 15 μm vertically, which gives spatial resolutions for *Y* and *Z* scans of ~60 and ~15 μm, respectively.

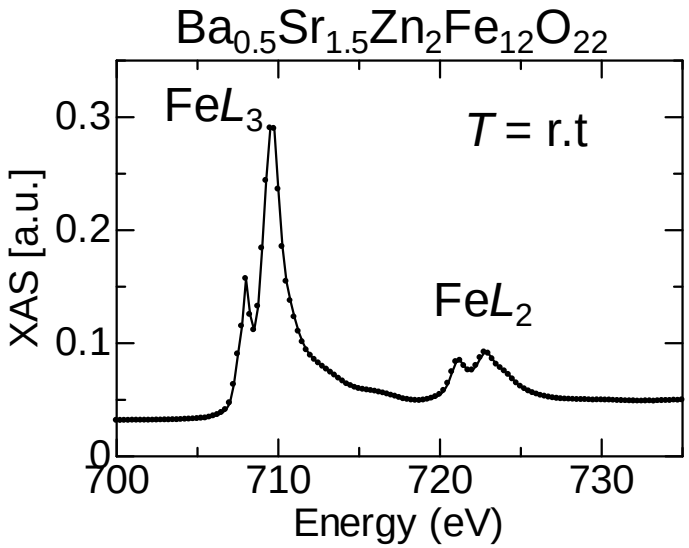

Figure 2.2 X-ray absorption spectra of ZnY(1.5) at room temperature.

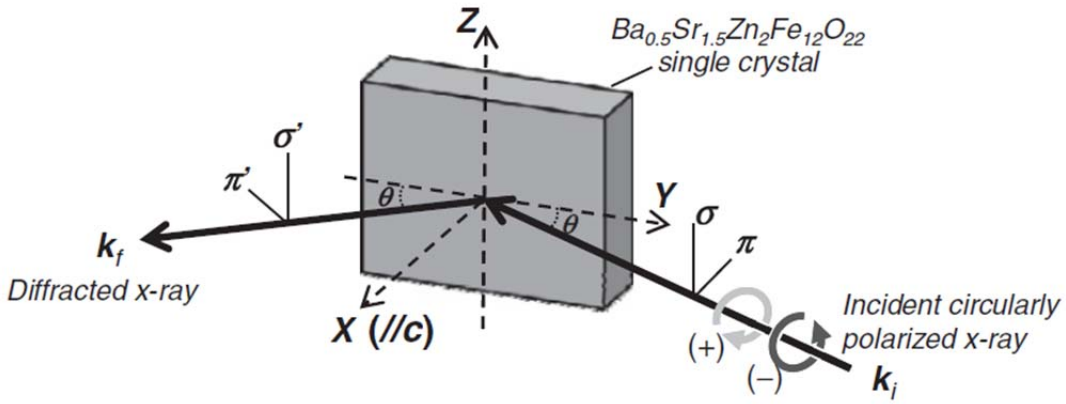

Figure 2.3 Schematic illustration of the scattering geometry. Here, k_i and k_f are the propagation vectors of the incident and diffracted X-rays, respectively, and θ denotes the Bragg angle. The σ and σ' components are perpendicular to the scattering plane, and the π and π' components are parallel to the scattering plane.

2.4.1. Magneto-electric (ME) cooling effects

For a ZnY(1.5) crystal, we performed a magneto-electric (ME) cooling in order to control the spin-chirality of the proper screw magnetic structure . Figure 2.4 (a) shows schematic illustrations of the setup for the ME cooling effects. The scattering geometry is as same as one of Fig. 2.3 but, on the ZnY(1.5) sample, electrodes are made by a sliver paste to apply electric field. To apply an electric field, a voltage source (Keithley 6517B) was used. To apply a magnetic field, a samarium-cobalt magnet, which enabled us to change the polarity of the magnetic field by rotating it, was used [Fig. 2.4(b)]. An applied magnetic field is estimated to 0.1 ~ 0.2 T. During the ME cooling, we inserted the samarium-cobalt magnet beneath the sample and increased the applying voltages gradually [Fig. 2.5(a)]. Figure 2.5(b) shows a picture of a scanned, rectangular-shaped, ZnY(1.5) crystal [2.2 × 2.4 mm^2] and geometric settings of the ME cooling. Directions of applied electric and magnetic fields are also shown. This crystal has a step by < ~ 0.1 mm and a hair seam. In order to avoid the step, domain scans after ME cooling are mainly conducted for upper region of the picture

ME cooling was performed by following procedure: cooling the sample from 330 K (> T_N) [see the section 5.1] to 40 K with increasing the applied voltage to ±500V (208kV/m) gradually, due to the low resistivity in high temperature. The electric fields remained applied while the measurements. A procedure of an applied electric field in a ME cooling is shown in table 2.2.

Temperature (K)	330	300	270	220	180	150	130	120	111	105	95	89	87	83	80
Applied electric field (kV/m)	2	3	3	6	15	38	63	83	88	104	125	146	167	188	208

Table 2.2 A procedure of an applied electric field in a ME cooling

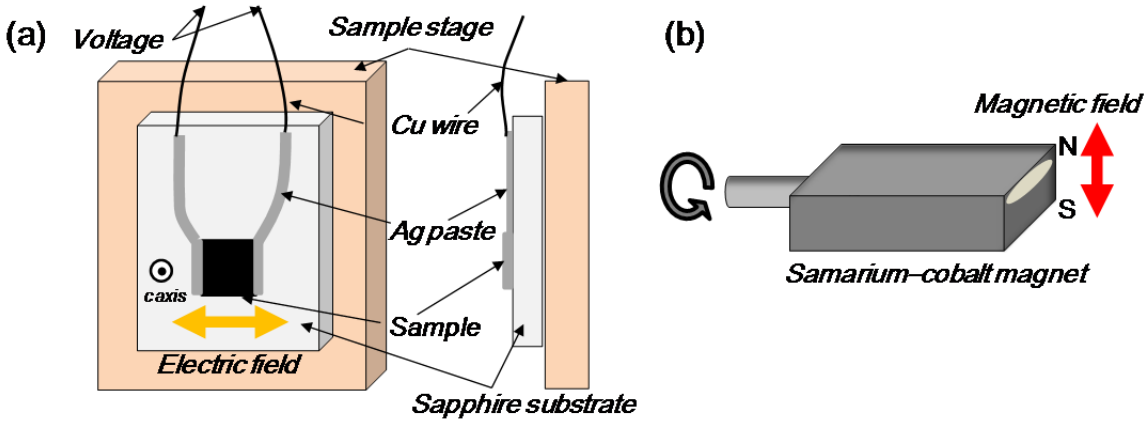

Figure 2.4 Schematic illustrations of (a) the setup for the magneto-electric cooling effects and (b) a magnet for applying a magnetic field to the sample.

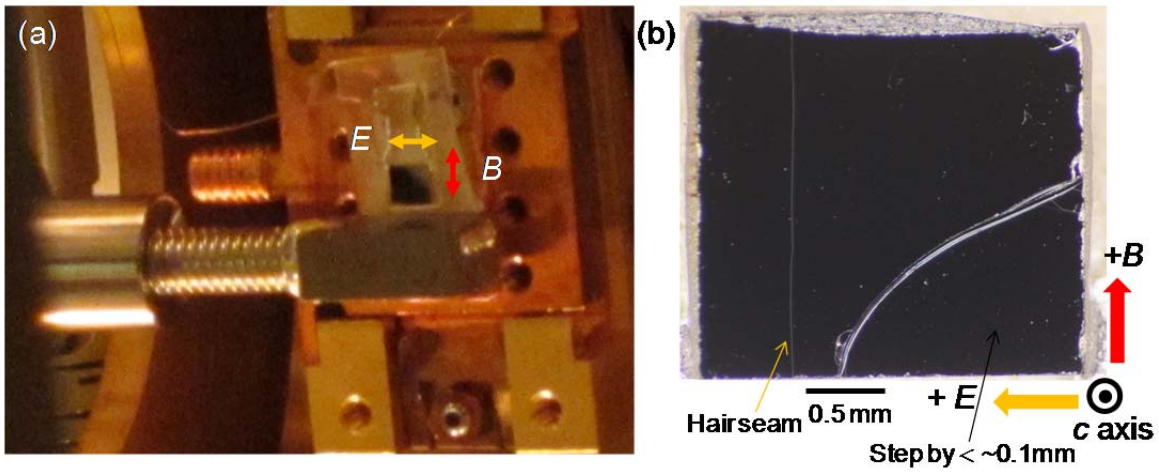

Figure 2.5 (a)A picture during a magneto-electric cooling for the ZnY(1.5) crystal. (b) a picture of a scanned ZnY(1.5) crystal [2.2 × 2.4 mm^2]. Directions of applied electric and magnetic fields are shown.

Chapter 3 Crystal growth of (Ba,Sr)CoZ single crystals.

In 2010, spiral-induced ferroelectricity above room temperature was discovered in polycrystalline $Sr_3Co_2Fe_{24}O_{41}$ [SrCoZ] samples4. One of the goals of my Ph.D. thesis was to grow single crystals of SrCoZ since the growth of single crystals of SrCoZ had not ever been reported. However, Sea Hwan Chun et al. reported the crystal growth of the $Ba_{3-x}Sr_xCoZ$ ($2.40 \leq x \leq 3.00$) and their multiferroic properties[61], before we did. In this chapter, we will introduce growth of the (Ba,Sr)CoZ single crystals by means of Na_2O-Fe_2O_3 flux. Following ref. 61, we tried to grow (Ba,Sr)CoZ single crystals, and optimized the flux condition to grow single crystals of SrCoZ. In addition, we will report BaCoZ single crystal growth by means of BaO –B_2O_3 flux.

3.1. Crystal growth of (Ba,Sr)CoZ crystals by Na_2O-Fe_2O_3 flux

In ref. 61, single crystals of the (Ba,Sr)CoZ were grown by the Na_2O-Fe_2O_3 flux method similar to that described in ref. 64. The molar percentage ratios of the chemicals were $BaCO_3$: $SrCO_3$: Co_3O_4 : Fe_2O_3 : Na_2CO_3 =22.66(1-*x'*) : 22.66*x'* : 7.555: 61.71 : 8.069. We put the mixture of these chemicals into a platinum crucible. Using a furnace, the mixture was heated to 1420 °C and kept at that temperature for 20 hours to melt the mixture completely. Subsequently, we conducted several thermal cycles to remove spinel nuclei and extra hexaferrites nuclei, and cooled the mixture from each growth temperature to below 1111°C, where the flux solidifies, at 0.2~0.5 °C/hour to grow single crystals. All the above processes were carried out in air. After these processes, the mixture was cooled down to room temperature. The obtained crystals were leached from the crucibles with hot dilute nitric acid. In Table 3.1, we list the condition of experimental (Ba,Sr)CoZ growth runs. Conditions 1 ~ 6 correspond to the above-mentioned conditions.

In Ba :Sr = 0 : 3 (no. 1 and 2) and 1 : 11.0798 (no. 3), we obtained the Z-type as a main phase with some of the U-, Y-, and M- types. As the ratio of Sr increases, SrCoZ crystals become stable. Comparing conditions 1 and 2, which are the same initial compositions but different cooling rate and growth temperature, Z-types are more stable in condition 2. Growth temperature and/or rate may also affect the resultant types, but further study is needed. Although size of the crystals is depend on the runs, a SrCoZ crystal with the typical dimension 3.1 × 2.6 × 1.0 mm^3 is obtained in condition 2. In addition, SrCoU crystals are also obtained [Fig 3.1 (c) and (d)]. This is the first reports of the single crystal growth of the SrCoU as far as we know.

It is reported that Z-type was sometimes found syntactically intergrown with Y- or U-type, since Z-, U- and Y- structures are closely related to each other. Actually, we observed many small pieces of the U-type in a crushed Z-type[62]. However, results of neutron diffraction technique show the intergrowth is negligible for the macroscopic measurements in carefully-chosen SrCoZ crystals by

means of a transmission Laue pattern by high-energy X-ray[63] and saturation magnetization in the whole crystal [Fig. 3.1 (a) and (b)].

To explore the more stable initial compositions for SrCoZ, we changed the ratio of (Ba,Sr) : Co to 3 : 2 and 2 :1 for Z type-obtained flux [Ba :Sr = 0 : 3 and 1 : 11.0798] with the compositions of Na_2CO_3 and Fe_2O_3 unchanged [Conditions 7 ~ 10]. It is worth noting that (Ba,Sr) : *Me* ratio in Z type $(Ba,Sr)_3Me_2Fe_{24}O_{41}$ is not 1 : 1 but 3 :2. However, no Z-type single crystals were obtained although a mixture of Z- and M- type was obtained as shown in Table 3.1

In summary, (Ba,Sr)CoZ single crystals become stable in the (Ba,Sr) : Co = 1 :1 plane for a Sr-richer Ba :Sr ratio than Ba :Sr = 1 : 11.0798.

Conditions	Initial composition (mole %)					Max. temp. (°C)	Growth temp. (°C)	Rate (°C/h)	Thermal cycling	Results	(Ba,Sr) : Co	Ba : Sr
	$BaCO_3$	$SrCO_3$	Co_3O_4	Fe_2O_3	Na_2CO_3							
No. 1	0.000	22.665	7.555	61.711	8.069	1420	1170	0.5	○	Z * 3, U*2, M * 4 , (U+M) *1	1: 1 plane	0 : 3
No. 2	0.000	22.665	7.555	61.711	8.069	1420	1175	0.2	○	Z * 10, U *1, M * 1, (Z+Y) * 1	1: 1 plane	0 : 3
No. 3	1.876	20.789	7.555	61.711	8.069	1420	1170	0.5	○	Y * 3, Z * 5,,U * 1, (Z+Y+U) * 2	1: 1 plane	1: 11.0798
No. 4	7.555	15.110	7.555	61.711	8.069	1420	1170	0.5	○	Y * 10	1: 1 plane	1 : 2
No. 5	15.110	7.555	7.555	61.711	8.069	1420	1170	0.5	○	Y * 10	1: 1 plane	2 :1
No. 6	22.665	0.000	7.555	61.711	8.069	1420	1170	0.5	○	Y * 5	1: 1 plane	3 :0
No. 7	0.000	26.866	5.970	59.328	7.836	1420	1170	0.5	○	(Z+M) * 1, U * 2	3:2 plane	0 :3
No. 8	2.224	24.642	5.970	59.328	7.836	1420	1170	0.5	○	Y * 3	3:2 plane	1: 11.0798
No. 9	0.000	28.467	4.745	58.686	8.102	1420	1180	0.5	○	U * 1, M * 2	2:1 plane	0 : 3
No. 10	2.357	26.111	4.745	58.686	8.102	1420	1180	0.5	○	Y * 3	2:1 plane	1: 11.0798

Table 3.1 Experimental (Ba,Sr)CoZ growth runs in the Na_2O-Fe_2O_3 flux system. Parentheses indicate the mixtures of the hexaferrites, e.g. (Z + Y) is the mixture of the Y-and Z-type.

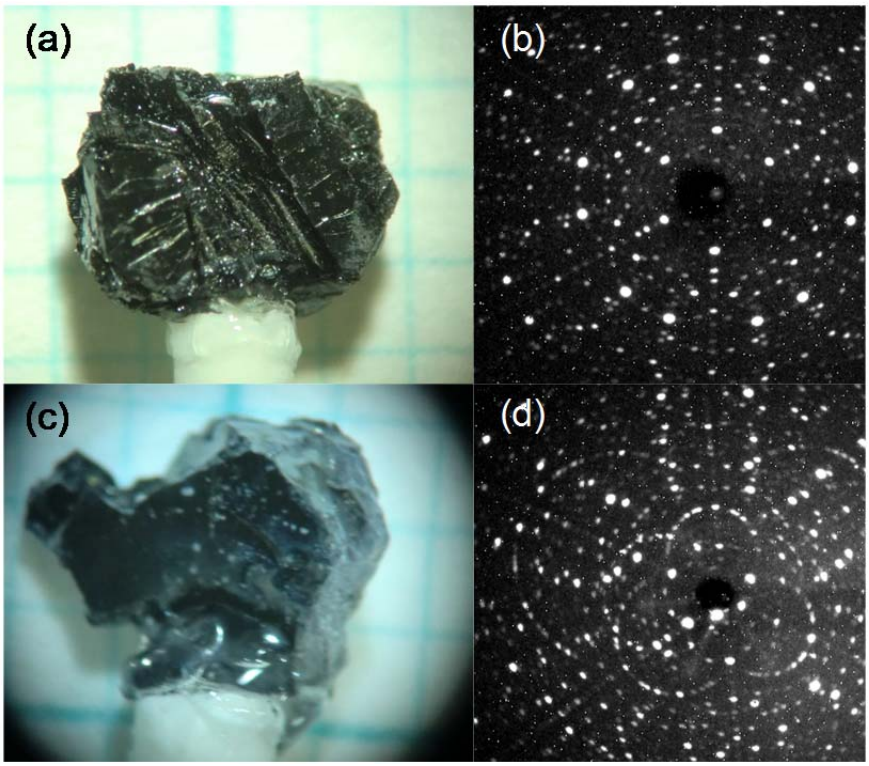

Figure 3.1 (a) a picture and (b) a transmission Laue pattern by a high-energy X-ray of a SrCoZ crystal. (c) a Picture and (d) a transmission Laue pattern by a high-energy X-ray of a

SrCoU crystal

3.2. Crystal growth of BaCoZ crystals by BaO –B_2O_3 flux

$BaO–B_2O_3$ flux is another flux which can grow Y-type hexaferrite. Single crystals growth of $Ba_2Zn_2Fe_{12}O_{22}$ was reported in *Me* = Zn system [59]. However there have been no experimental reports in *Me* = Co system. As Y-type hexaferrites are structurally close to Z-type hexaferrites, crystal growth of Z- type is expected in this flux. In this section, we will report BaCoZ single crystal growth by means of the BaO –B_2O_3 flux. In Table 3.2 we list the condition of experimental BaCoZ growth runs and the results.

The initial composition and thermal process of the $BaO–B_2O_3$ flux is decided by using ref. 59. A ratio of Co : Fe in the initial composition should be 1 :12, considering the chemical formula of Z-type $Ba_3Co_2Fe_{24}O_{41}$. We put the mixture of these chemicals into a platinum crucible. Using a furnace, the mixture was heated to 1300 °C and kept at that temperature for 24 hours to melt the mixture completely. Subsequently, we cooled the mixture from 1300°C to 1000°C, at 0.75 °C/hour to grow single crystals. All the above processes were carried out in air. After these processes, the mixture was cooled down to room temperature. The obtained crystals were leached from the crucibles with hot dilute nitric acid.

As a result, we successfully obtained BaCoZ single crystals with a typical dimension 3.2 × 3.0 × 1.2 mm^3 in the $BaO–B_2O_3$ flux [Fig 3.2 (a)]. As we discussed in section 3.1, growth of BaCoZ single crystals in Na_2O-Fe_2O_3 flux is difficult although there are a few reports of single crystal growth of BaCoZ single crystals as a secondary phase[57]. However in the BaO-B_2O_3 flux, BaCoZ became stable and the region seems to be wide. This compensates for shortcomings of the Na_2O-Fe_2O_3 flux.

Conditions	Initial composition (mole %)				Max. temp. (°C)	End temp. (°C)	Rate (°C/h)	Results
	B_2O_3	$BaCO_3$	CoO	Fe_2O_3				
No. 1	18.556	46.91	4.933	29.601	1300	1000	0.75	Y*4
No. 2	17.546	44.357	5.442	32.655	1300	1000	0.75	Y*3、Z*1
No. 3	16.641	42.067	5.899	35.393	1300	1000	0.75	Z*3
No. 4	15.084	38.131	6.684	40.102	1300	1000	0.75	Z*3

Table 3.2 Experimental BaCoZ growth runs and results in the $BaO–B_2O_3$ flux system.

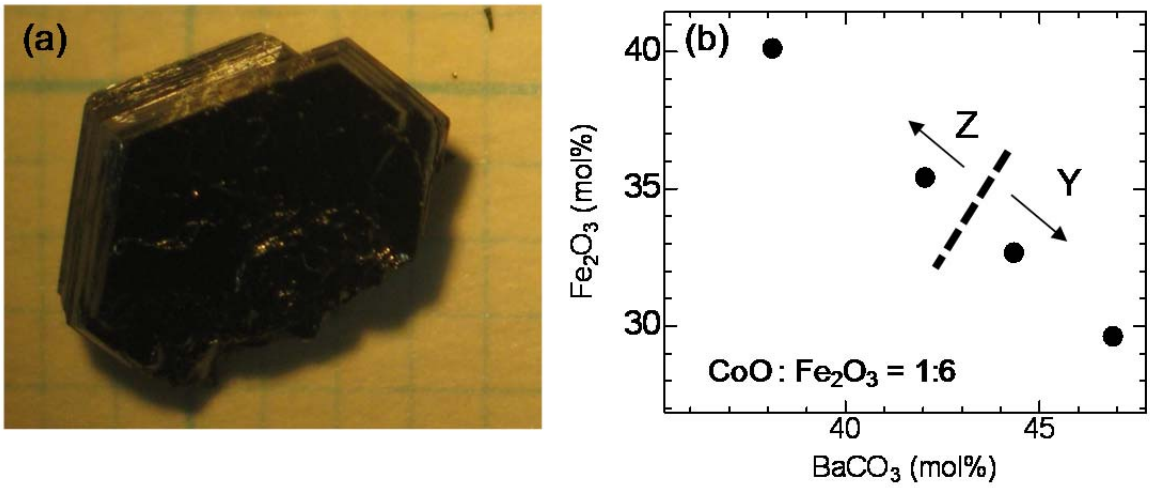

Figure 3.2 (a) a picture of a BaCoZ crystal. (b) Single-crystal fields in the BaO-B_2O_3 flux. Conditions in Table 3.2 are plotted. Z and Y indicate $Ba_3Co_2Fe_{24}O_{41}$ and $Ba_2Co_2Fe_{12}O_{22}$, respectively.

3.3. Summary of this chapter

We tried to grow (Ba,Sr)CoZ single crystals, and optimized the flux condition to grow (Ba,Sr)CoZ single crystals by means of the Na_2O-Fe_2O_3 flux and the $BaCO_3$-B_2O_3 flux.

In the Na_2O-Fe_2O_3 flux, we found (Ba,Sr)CoZ single crystals become stable in the (Ba,Sr) : Co = 1 :1 plane for a Sr-richer Ba :Sr ratio than Ba :Sr = 1 : 11.0798.

In the $BaCO_3$-B_2O_3 flux, we successfully obtained the BaCoZ single crystals which are difficult to grow in the Na_2O-Fe_2O_3 flux.

Chapter 4 Multiferroic properties of $Ba_{2-x}Sr_xNi_2Fe_{12}O_{22}$ [NiY(x)]

As we mentioned in chapter 1, some Y-type hexaferrites show multiferroic properties. We observed multiferroic properties in the *Me* = Ni system in Y type $(Ba,Sr)_2Me_2Fe_{12}O_{22}$, and examined its origin by means of neutron diffraction techniques. Although a sample for measurements of resonant circular x-ray diffraction (RcXRD) requires to have an ultra-flat surface due to the surface-sensibility of the experiment, the surface of a NiY(1.5) was insufficient. We tried to improve the quality of crystal by changing the growth condition. In this chapter, we will introduce our work on a new magnetoelectric Y-type hexaferrite system, NiY(x).

4.1. Crystal growth and an annealing condition

Single crystals of NiY(x) were grown by a Na_2O-Fe_2O_3 flux method similar to that described in ref. 64, which reports the growth of $Ba_{0.5}Sr_{1.5}Zn_2Fe_{12}O_{22}$ [ZnY(1.5)]. In ref. 64, the molar percentage ratios of the starting chemicals were BaO: SrO: ZnO: Fe_2O_3: Na_2O = 19.69(1-*x'*): 19.69*x'*: 19.69: 53.61: 7.01. We followed these ratios but replaced ZnO with NiO. Thus, in the NiY(x) study, the ratios of the starting chemicals were 19.69(1-*x'*) $BaCO_3$, 19.69*x'* $SrCO_3$, 19.69 NiO, 53.61 Fe_2O_3, and 7.01 Na_2CO_3. The resulting chemicals were mixed, packed into platinum crucibles, and covered by platinum caps. For *x*=0 samples, the chemicals were first heated to 1420 °C, kept at that temperature for 20 hours, and then cooled to 1000 °C at a rate of 0.8 °C/h to grow crystals. Meanwhile, for $x \neq 0$ samples, the chemicals were first heated up to 1420 °C and cooled to 1350 °C over a 24-hour period.. Subsequently, they were cooled down to 990 °C at a rate of 0.75 °C/h to grow crystals. All the above processes were carried out in air. The obtained crystals were leached from the crucibles with hot dilute nitric acid, and had typical dimensions of ~4×5×3 mm^3 (for x = 1.5). The chemical compositions for some of the crystals were analyzed by the inductively coupled plasma (ICP) technique. A typical result for an x = 1.5 crystal was Ba : Sr : Ni : Fe = 0.44 : 1.41 : 1.99 : 12.00, which ensured that the relation between the starting and the resulting compositions in ref. 64 was satisfied even if ZnO was replaced by NiO. The obtained crystals were hexagonal-shaped plates with flat surfaces normal to the *c* axis. The appearance of the obtained crystal depends on Sr concentration *x*. As *x* increased, the crystals become porous with crumbling and ambiguous surfaces, which suggests that the quality of the crystals becomes low. We did not succeed in growing the crystals with $x > 1.5$. These results may be ascribed to an increase in the viscosity of the flux due to the increase of Sr concentration *x*[64]. Most of the measurements in this chapter use as-grown samples. However, to test the effect of a post-annealing on the magnetic and magnetoelectric properties, an x = 1.5 crystal was annealed in the following

procedure. After holding the crystal at 900 °C for 8 days, it was cooled to room temperature at a rate of 50 °C/h under oxygen flow. This procedure followed that of ref. 65, which is an optimal condition to enhance the resistivity of a Y-type hexaferrite $Ba_{0.5}Sr_{1.5}Zn_2Fe_{12}O_{22}$.

A sample for measurements of resonant circular X-ray diffraction (RcXRD) (in chapter 5) is required to have an ultra-flat surface due to the surface-sensibility of the experiment. Therefore, NiY(1.5) crystals for RcXRD were grown by a different thermal process from that mentioned above. The mixture of starting chemicals was heated to 1420 °C and kept at that temperature for 20 hours to melt the mixture completely. Subsequently, we conducted several thermal cycles to remove spinel nuclei and extra hexaferrite nuclei, and cooled the mixture from 1180 °C to 1100 °C at 0.2 °C/hour to grow single crystals. As a result of the thermal process, the quality of obtained crystals was drastically improved [Figure 4.1]. We used the obtained NiY(1.5) crystals for RcXRD [see also chapter 5] .

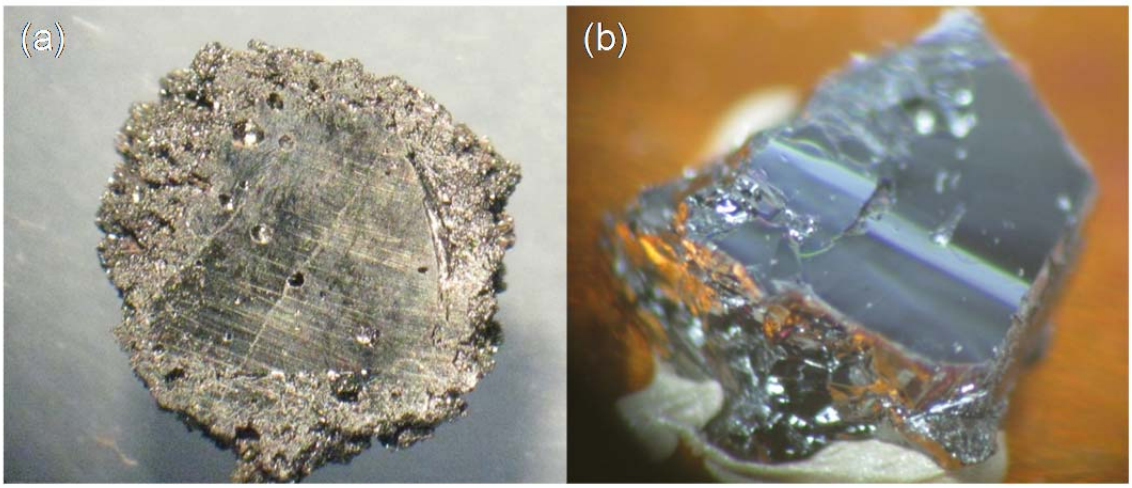

Figure 4.1 Pictures of NiY(1.5) crystals grown by the thermal processes (a) without the thermal cycling and (b) with the thermal cycling. The crystal of (a) was cut to show the internal pores.

Next, we changed the initial composition of the flux and grew the NiY(1.5) crystals. Table 4.1 shows the three different growth conditions and their results in addition to the above-mentioned conditions. In condition 1 we successfully obtain the high quality NiY(1.5) crystal as shown in Fig 4.1(b), although in condition 2 and 3 the measurable crystals were not obtained. The thermal cycling processes are an effective way to have an ultra-flat surface in hexaferrite materials. Conditions 2 and 3 constitute of much amount of Fe_2O_3 components than that successful ones, which indicate Fe_2O_3 also, not only $SrCO_3$, may affect the viscosity of the flux. The properties of NiY(1.5) grown by condition 1. is shown in subsection 4.2.6.

	Initial composition (mole %)					Max. temp. (°C)	Growth temp. (°C)	Rate (°C/h)	Thermal cycling	Results
	$BaCO_3$	$SrCO_3$	NiO	Na_2CO_3	Fe_2O_3					
NiY(x = 0)	19.69(1-x)	19.69x'	19.69	7.01	53.61	1420	1420	0.8	No	Only Y
NiY(x ≠ 0)						1420	1350	0.75	No	Only Y
NiY(1.5) [For RcXRD]	2.9535	16.7365	19.69	7.01	53.61	1420	1180	0.2	Yes	Only Y
No. 1	2.624988	14.87493	17.49992	10.00011	55.00005	1420	1190	0.2	Yes	Only Y
No. 2	2.474654	14.02304	16.4977	10.00419	57.00042	1420	1180	0.2	Yes	No measurable crystals
No. 3	2.474976	14.02486	16.49984	8.000201	59.00012	1420	1190	0.2	Yes	No measurable crystals

Table 4.1 Experimental NiY(x) growth runs in the Na_2O-Fe_2O_3 flux system.

4.2. Experimental results and discussion

4.2.1. Lattice constants and magnetic transition temperatures

We confirmed that the obtained crystals have the Y-type hexaferrite structure by measuring the lattice constants. Ref. 64 reports that lattice constants a and c in $Ba_{2-x}Sr_xZn_2Fe_{12}O_{22}$ system are a linear function of Sr concentration x. Figure 4.2(b) shows the relation between x and the lattice constants a and c at room temperature for the obtained crystals. With increasing x, i.e., the concentration of Sr whose ionic radius is smaller than that of Ba, both a and c decrease linearly. The result suggests that the Sr concentration in the obtained crystals has been successfully controlled. Figure 4.3 (a) shows the temperature T dependence of the in-plane magnetization M of $Ba_{2-x}Sr_xNi_2Fe_{12}O_{22}$ crystals with x = 0, 0.25, 0.5, 0.75, 1.0, 1.25, and 1.5. The measurements were carried out in a magnetic field of B = 0.01 T. All the crystals show a steep increase of M at around 650 – 660 K, suggesting that a ferrimagnetic ordering occurs at those temperatures. Inverted triangles in Figure 4.3 (a) denote the transition point from the ferrimagnetic ordered state to an antiferromagnetic ordered state which is ascribed to the formation of screw magnetic order, as described below. These ordering and transition temperatures are plotted in Figure 4.3 (b), as a magnetic phase diagram for the $Ba_{2-x}Sr_xNi_2Fe_{12}O_{22}$ system in the T-x plane. In $x \leq 0.5$ crystals, the ferrimagnetic phase remains down to the lowest temperature. In $x > 0.5$ crystals, the transition temperature from the ferrimagnetic to the antiferromagnetic ordered state is observed and monotonically increases with increasing x. This result indicates that the screw magnetic ordered states are stabilized by Sr-substitution. Meanwhile, the ferrimagnetic ordering temperature is less x-dependent but decreases slightly with increasing x.

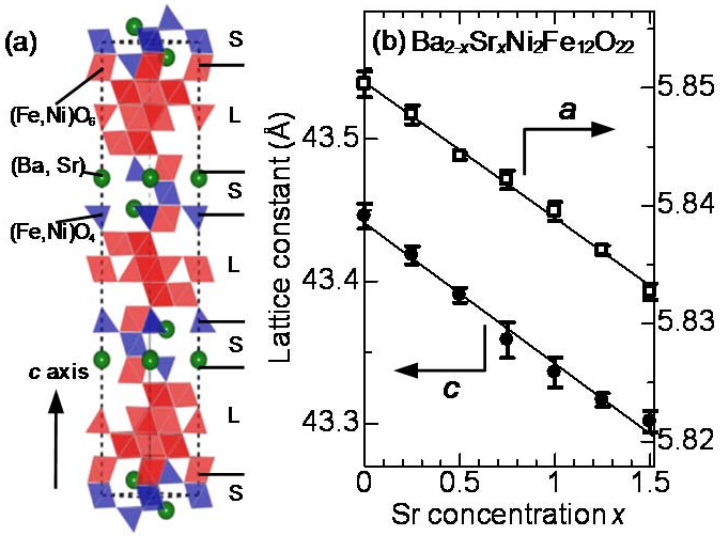

Figure 4.2 (a) Schematic crystal structure of $Ba_{2-x}Sr_xNi_2Fe_{12}O_{22}$. The magnetic structure consists of alternate stacks of spin bunches of L (red) and S (blue) blocks, along the hexagonal *c* axis, having large and small magnetic moments, respectively. (b) The lattice constants *a* (open squares) and *c* (closed circles) at room temperature as a function of Sr concentration *x*.

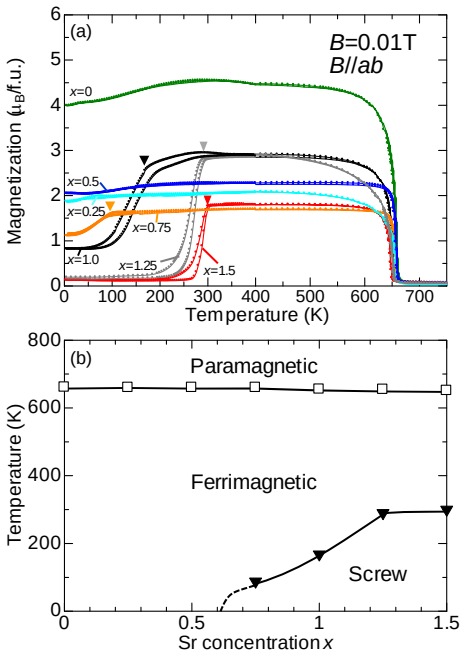

Figure 4.3 (a) Temperature dependence of in-plane magnetization of $Ba_{2-x}Sr_xNi_2Fe_{12}O_{22}$ crystals with x = 0, 0.25, 0.5, 0.75, 1.0, 1.25, and 1.5. The measurements were carried out at

0.01 T. Inverted triangles denote the transition point from the ferrimagnetic to screw magnetic ordered state for the respective crystals. (b) Magnetic phase diagram for the $Ba_{2-x}Sr_xNi_2Fe_{12}O_{22}$ system in the *T*-*x* plane. Open squares and closed inverted triangles denote the Néel temperature and the ferrimagnetic-screw transition points, respectively.

4.2.2. Sr-concentration dependence on magnetically-induced ferroelectricity

Figure 4.4 shows the *B* dependence of (a) the in-plane magnetization and (b) the electric polarization for selected $Ba_{2-x}Sr_xNi_2Fe_{12}O_{22}$ crystals at 20 K. The thick bars indicate magnetic transitions. The inset of Fig. 4.4 shows a schematic experimental configuration for the measurement of the electric polarization. Before the measurement, each crystal was electrically poled by applying an electric field with changing *B* from a paraelectric phase to a *B*-induced ferroelectric phase. A previous neutron diffraction study[66] proposed that $Ba_2Ni_2Fe_{12}O_{22}$ (x = 0) shows a transverse conical spin structure which allows a finite polarization. However, our crystals with $x \leq 0.5$ appear to be simply ferrimagnetic [Figure 4.3 (a) and Figure 4.4 (a)] and not ferroelectric [Figure 4.4 (b)]. For the x = 0.75 and 1.0 crystals, distinct suppression of the low-field magnetization was observed below 88 K and 168 K, respectively [Figure 4.3(a)], which suggests a transition into a screw magnetic order. However, their *M*-*B* curves at 20 K exhibit simply ferrimagnetic behaviors, as seen in Figure 4.4 (a). Furthermore, they show little magnetoelectric effect at 20 K, as displayed in Figure 4.4 (b). we thus speculate that the ferrimagnetic and screw ordered phases coexist in x = 0.75 and 1.0 crystals and that the former contribution is predominant in the *M*-*B* and *P*-*B* curves. In x = 1.25 and 1.5 crystals, distinct magnetoelectric effects accompanied by magnetization anomalies were observed. As seen in Fig. 4.4(a), the magnetization of x = 1.25 and 1.5 increases in a stepwise fashion with increasing *B*, and two or three distinct anomalies [marked by thick bars in Fig. 4.4 (a)] were observed in their magnetization curves. Corresponding to these magnetization anomalies, anomalies in the electric polarization were also observed, as displayed in Fig. 4.4(b). Though no finite electric polarization was observed at B = 0, the electric polarization develops at the magnetic field where the second (first) magnetization step appears at x = 1.25 (x = 1.5). With increasing *B*, the electric polarization shows the maximum and then decreases. At the magnetic field where the magnetization is saturated, the electric polarization disappears. These features are essentially the same as those observed in other magnetoelectric Y-type hexaferrites such as $Ba_{0.5}Sr_{1.5}Zn_2Fe_{12}O_{22}$ [38] and $Ba_2Mg_2Fe_{12}O_{22}$ [43,44]. Thus, it is possible to consider that the *paraelectric* "proper" screw ordered state at B = 0 transforms into a collinear ferrimagnetic state via some intermediate state(s) which may be ferroelectric transverse conical magnetic ordered phase(s). In the following subsections, we focus on the x = 1.5 crystal showing the largest electric polarization and discuss its magnetically-induced ferroelectricity.

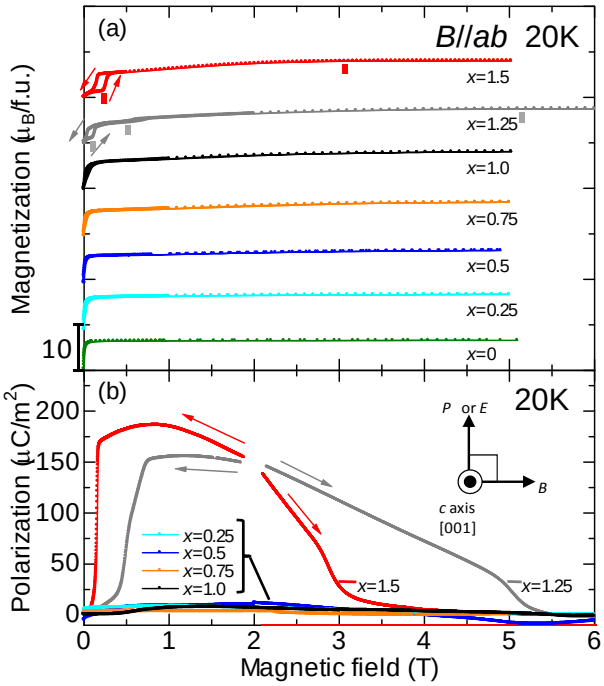

Figure 4.4 Magnetic-field dependence of (a) the in-plane magnetization and (b) the electric polarization for selected $Ba_{2-x}Sr_xNi_2Fe_{12}O_{22}$ crystals at 20 K. The inset shows a schematic experimental configuration. The magnetization data in (a) are vertically offset for clear comparison.

4.2.3. Magnetically-induced ferroelectricity and magnetism in $x = 1.5$ crystal

Figure 4.5 shows the B dependence of (a) in-plane magnetization, (b) relative permittivity, and (c) electric polarization in the $x = 1.5$ crystal at 20 K. Thick bars in Figs. 4.5 (a), 4.5 (b), and 4.5 (c) indicate magnetic transitions, permittivity anomalies, and edges of polarization, respectively. Two metamagnetic transitions appear in the isothermal magnetization curve, and accompany the permittivity anomalies. A substantial electric polarization is evident only in the intermediate phase at 0.2 T $\leq B \leq$ 3.0 T, named intermediate I. The permittivity anomaly at 0.2 T shows a step-like behavior while that at 3.0 T exhibits a divergent tendency. This suggests that the transitions at the lower and the higher B are a first and a second order-like transition, respectively. The transition natures are also consistent with the result of the P-B curve in which the electric polarization shows a discontinuous jump and a gradual disappearance at the low- and the high-B transitions, respectively. The value of linear ME effect coefficient α is 1.0×10^{-8} [sm^{-1}] at $H = 0.16$ T, which is a relatively high value, compared to $\alpha = 4 \times 10^{-12}$ sm^{-1} in Cr_2O_3(Typical electro-magnetic material[67]) or $2.5 \times 10^{-10} sm^{-1}$[SrCoZ in ref. 4]. Figure 4.6 shows the B dependence of (a) in-plane magnetization and (b) electric polarization of the $x = 1.5$ crystal at selected temperatures. At

temperatures below 100 K, we observed *B*-induced electric polarization, i.e., magnetoelectric effect. The largest electric polarization (2×10^2 μC/m^2) emerges at 10 K. Figure 4.6 (c) shows a magnetic phase diagram for the x = 1.5 crystal in the *T*-*B* plane, in which magnetic transitions observed in *B*-increasing runs are plotted [The thick bars in Fig. 4.6 (a)]. In addition to the ferroelectric intermediate I phase, another intermediate phase, named intermediate II, appears above 77 K. However, the electric polarization in the intermediate II phase is negligibly small. Although the ferroelectric intermediate I phase is sustained up to 250 K, we did not succeed in observing the electric polarization at T > 100 K due to its leaky behavior.

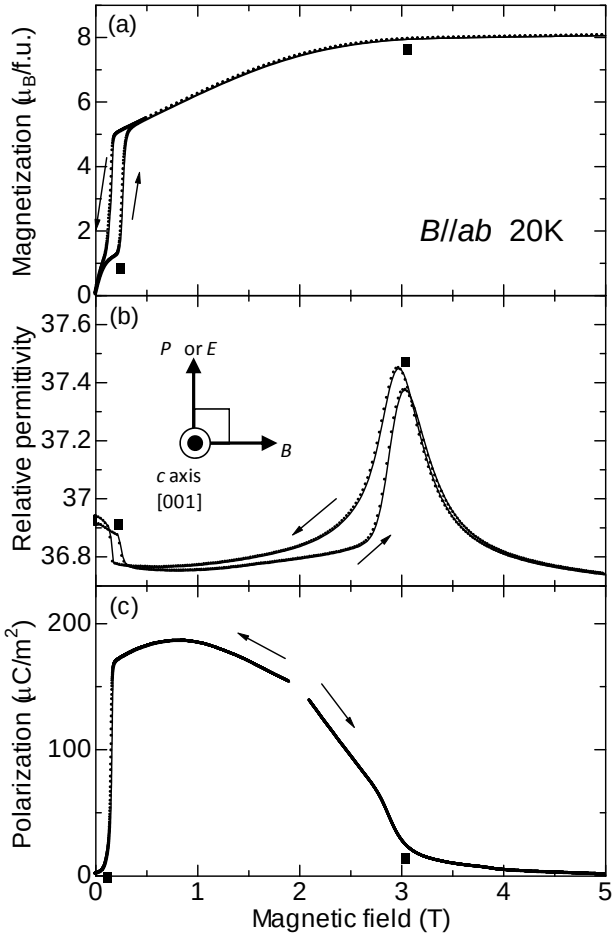

Figure 4.5 Magnetic-field dependence of (a) the in-plane magnetization, (b) relative permittivity, and (c) electric polarization in an x = 1.5 crystal at 20 K.

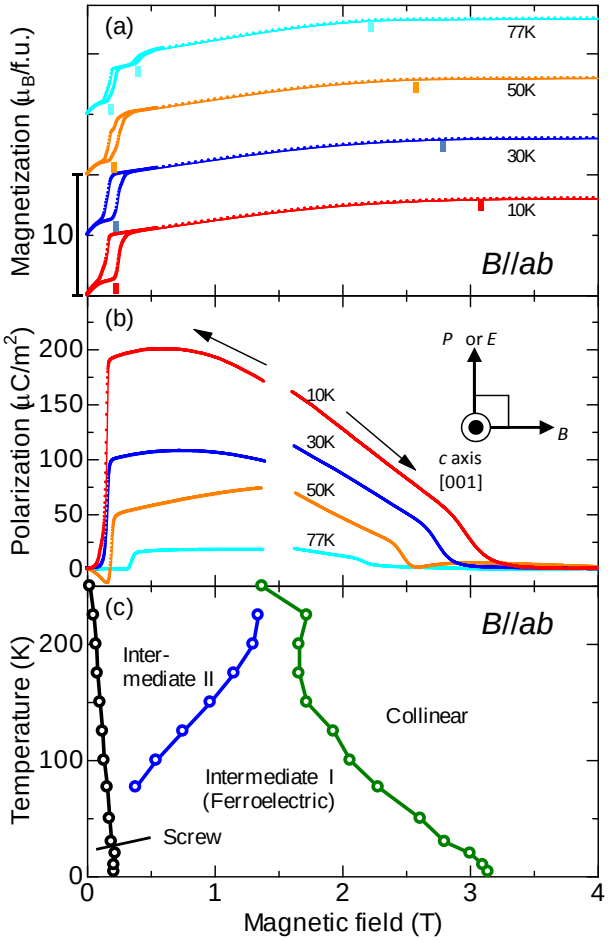

Figure 4.6 Magnetic-field dependence of (a) in-plane magnetization and (b) electric polarization of an x = 1.5 crystal at selected temperatures. (c) Magnetic phase diagram for the x = 1.5 crystal in the T-B plane. The magnetization data in (a) are vertically offset for clear comparison.

4.2.4. Neutron diffraction studies on x = 1.5

To confirm the screw magnetic structure at B = 0 and investigate magnetic structures of the intermediate I and II phases, we performed neutron diffraction measurements on an x = 1.5 crystal. Figure 4.7 (a) shows the L-scan profiles of (1 0 L) without external magnetic fields at selected temperatures between 10 and 300 K for the x = 1.5 crystal. In addition to the nuclear fundamental (1 0 1) reflection, incommensurate satellite (1 0 1±δ) reflections were observed at T < 300K. The (1 0 1±δ) reflections can be ascribed to a proper screw magnetic structure characterized by wave vector k_{IC} = (0, 0, δ). Because ferromagnetic components are absent in the proper screw magnetic structure, we assumed the fundamental (1 0 1) reflection at T < 300 K is due only to nuclear contribution. The inset of Fig. 4.7 (b) shows a proposed model for the proper screw magnetic

structure of $Ba_{2-x}Sr_xNi_2Fe_{12}O_{22}$, which is similar to those of $Ba_{0.5}Sr_{1.5}Zn_2Fe_{12}O_{22}$[38] and $Ba_2Mg_2Fe_{12}O_{22}$[68,69]. Red and blue arrows indicate spin bunches consisting of magnetic moments in the L and S blocks [See Fig. 4.2(a) and subsection 1.3]. When alternately stacked up along the *c* axis, the L and S spin bunches rotate by $\pi+\Phi_0/2$, where a turn angle Φ_0 of the screw is defined by $2\pi\delta/3$. At 300 K, the (1 0 1±δ) magnetic reflections disappear while the intensity of the (1 0 1) reflection increases. This means that there is a magnetic transition into a magnetic phase characterized by the wave vector k_0 = (0, 0, 0) between 250 K and 300 K. Figure 4.7 (b) shows *T* dependence of the turn angle Φ_0 calculated from the (1 0 1-δ) magnetic reflection. The value of Φ_0 shows little *T* dependence below 100 K (Φ_0 = 100° ~ 105°). As *T* is increased, Φ_0 starts to decrease above ~100 K. As *T* further increases, Φ_0 steeply drops above 250 K and becomes zero at 300 K. This means that the screw magnetic structure transforms into a collinear ferrimagnetic structure at 300 K. This behavior is consistent with the result of the *M*-*T* curve [See Fig. 4.3(a)] where the magnetization emerges at around 300 K. Figure 4.8 shows the *L*- scan profiles of the (1 0 *L*) at (a) 10 K and (b) 100 K for the *x*=1.5 crystal at *B* = 0, 0.3, 0.5, and 0.8 T along the *b* axis. Corresponding magnetic phases obtained from the phase diagram [Fig. 4.6(c)] are written on the respective data. IM-I and IM-II stand for the intermediate I and II, respectively. By applying *B*, the (1 0 1±δ) magnetic reflections disappear, and the (1 0 -1/2) magnetic reflection characterized by $k_{3/2}$ = (0, 0, 3/2) appears in the intermediate I and II phases. In addition, the intensity of the (1 0 1) reflection increases in the intermediate phases. This indicates that both the intermediate I and II phases are characterized by the same wave vectors k_0 = (0, 0, 0) and $k_{3/2}$ = (0, 0, 3/2). Note that magnetic structures in ferroelectric phases of other multiferroic Y-type hexaferrites $Ba_{0.5}Sr_{1.5}Zn_2Fe_{12}O_{22}$ and $Ba_2Mg_2Fe_{12}O_{22}$ are also characterized by the same wave vectors k_0 and $k_{3/2}$[68,69]. At 10 K and 0.3 T, the (1 0 1-δ) and (1 0 -1/2) magnetic reflections in addition to the increase of the intensity of the (1 0 1) reflection coexist, suggesting that the screw magnetic and intermediate I phases coexist. This probably reflects the nature of the first order-like transition at the phase boundary [See the low-*B* transition shown in Fig. 4.5]. Figure 4.9(a) shows *T* dependence of intensity of the (1 0 1) and the (1 0 -1/2) reflections at *B* = 0.8 T. A dashed line represents the boundary of the intermediate I and II [See also Fig. 4.6(c)]. The intensity of the (1 0 1) reflection decreases from the intermediate I to the intermediate II, whereas the intensity of the (1 0 -1/2) magnetic reflection increases from the intermediate I to the intermediate II. This reflects the decrease of the ferromagnetic component and the change in the helical component from the intermediate I to the intermediate II. Taking into account the appearance of distinct electric polarization in the intermediate I, it is reasonable to regard the intermediate I as a transverse conical magnetic phase. Figure 4.9(b) shows a possible magnetic structure of the intermediate I, which is the same as that proposed for a ferroelectric phase in another magnetoelectric Y-type hexaferrite $Ba_2Mg_2Fe_{12}O_{22}$[69]. It is worth mentioning that the length in the *c*-direction of the

magnetic unit cell with $k_{3/2}$ is 2/3 of the chemical unit cell. Therefore, this magnetic structure consists of a sequence of LSLS stacking.(see also section 1.3) In $Ba_2Mg_2Fe_{12}O_{22}$, a similar change in the intensity of a magnetic reflection is observed at a phase boundary between two transverse-conical magnetic phases[69]. In $Ba_2Mg_2Fe_{12}O_{22}$, it is proposed that the change is ascribed to the 90 ° rotation of spin bunches in the respective L and S blocks. For the present case, the intensity change of the (1 0 -1/2) magnetic reflection can be explained by this proposal. Note that the (1 0 *L)* scan around $L = 0$ mainly reflects the projection of the (1 0 0) plane in spins since lattice constant *c* is much longer than that of *a* [See Fig. 4.2(b)]. However, this proposal cannot explain the behavior of the (1 0 1) reflection and the negligible value of electric polarization in the intermediate II. Additional experiments are needed to clarify the magnetic structures of the intermediate I and II.

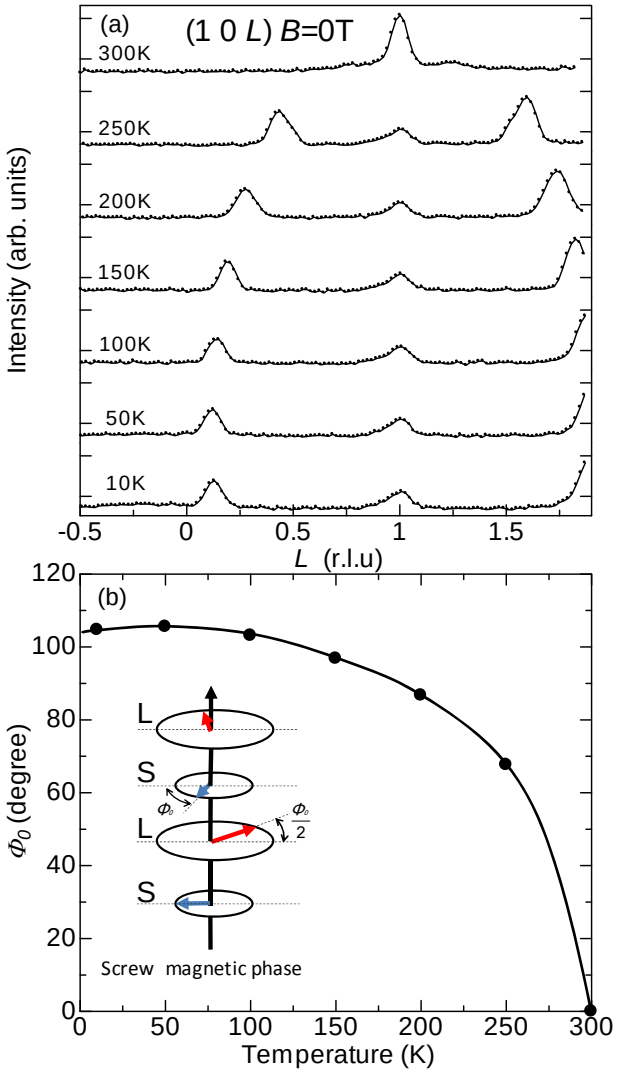

Figure 4.7 (a) The *L*-scan profiles of (1 0 *L*) in the absence of external magnetic fields at selected temperatures between 10 and 300 K for the $x = 1.5$ crystal [Intensities are plotted in

a logarithmic scale.]. (b) Temperature dependence of turn angle Φ_0 calculated from the magnetic satellite peak for the x = 1.5 crystal. The inset shows a proposed screw magnetic structure.

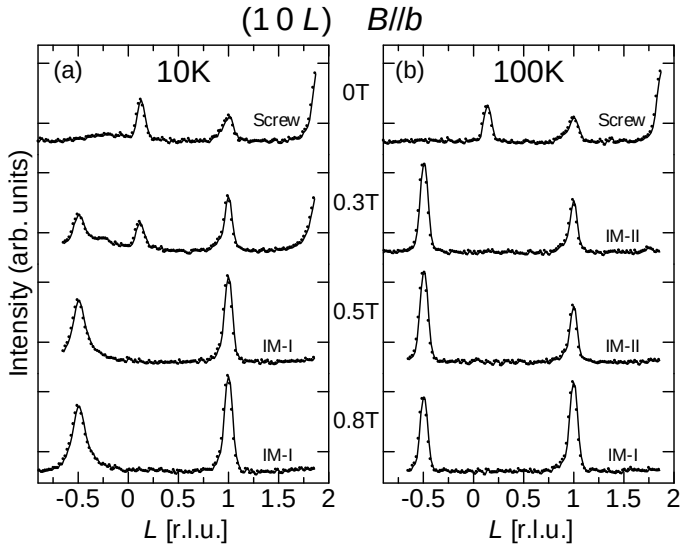

Figure 4.8 The L- scan profiles of (1 0 L) at (a) 10 K and (b) 100 K for the x = 1.5 crystal at B = 0, 0.3, 0.5, and 0.8 T [Intensities are plotted in a logarithmic scale.]. IM-I and IM-II stand for the intermediate I and II, respectively.

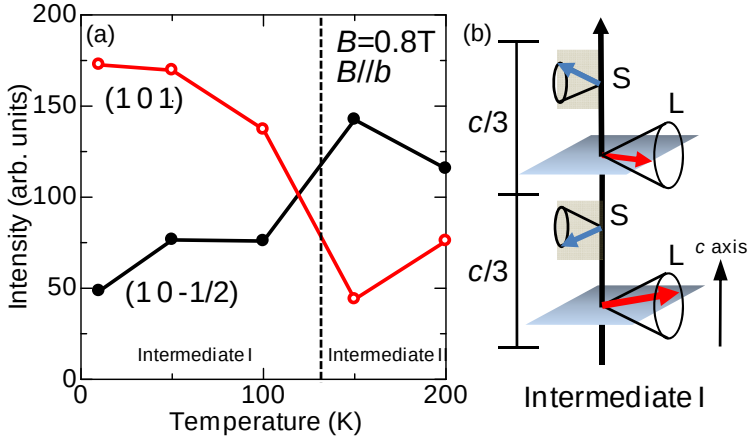

Figure 4.9 (a) Temperature dependence of intensity of the (1 0 1) and the (1 0 -1/2) reflections at B = 0.8 T. Dashed lines indicate the boundary between the intermediate I and II phases. (b) A possible magnetic structure of the intermediate I phase.

4.2.5. Annealing effect for x = 1.5 crystal

To improve the leaky behavior which prevents magnetoelectric measurements above ~100 K, we annealed the $x = 1.5$ crystal under the condition described in section 4.1. As a result, an increase of resistivity $\rho(T)$ was observed. [ρ(300 K) ~ 1.4 kΩ·cm for an as-grown crystal and ~1.5 MΩ·cm for an annealed crystal]. The drastic increase of the resistivity can be attributed to the removal of oxygen deficiency by the annealing under an oxygen flow.

Figure 4.10 shows B dependence of (a) in-plane magnetization and (b) electric polarization of the annealed $x = 1.5$ crystal at selected temperatures. The behavior of the M-B curves is similar to that of the as-grown crystal above ~77 K [Fig. 4.6(a)], and undergoes three metamagnetic transitions. Therefore, while the as-grown crystal involves the intermediate II phase only above ~77 K, the annealed crystal involves this phase at all the measured temperatures. The discontinuous jump in P-B curves at low B in the as-grown crystal becomes somewhat gradual by the annealing. This is apparently caused by the fact that the low-B transition does not occur between the screw and intermediate I phases but between the intermediate I and II phases. The largest electric polarization emerges at 30 K (1.6×10^2 μC/m^2). The value is comparable to that of the as-grown crystal. Figure 4.10(c) shows the magnetic phase diagram for the as-grown (dashed lines [the same as in Fig. 4.6(c)]) and the annealed (solid lines) $x = 1.5$ crystals.

In this diagram, magnetic transitions observed in B-increasing runs are plotted [The thick bars in Figs. 4.6(a) and 4.10(a)]. Both the boundaries (intermediate II → intermediate I and intermediate I → collinear) are shifted to higher magnetic fields. The ferroelectric intermediate I phase is sustained up to ~250 K. Because of the enhancement of $\rho(T)$ by the annealing, we succeeded in observing the electric polarization up to T ~175 K, which is higher than that of the as-grown crystal.

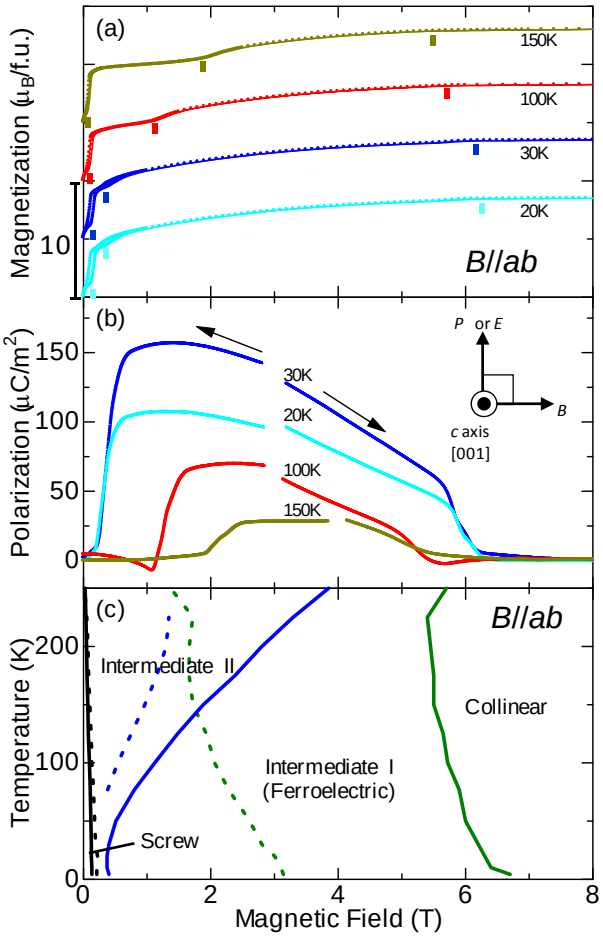

Figure 4.10 Magnetic-field dependence of (a) in-plane magnetization and (b) electric polarization at selected temperatures for an annealed x = 1.5 crystal. (c) Magnetic phase diagram for as-grown (dashed lines) and annealed (solid lines) x = 1.5 crystals. The magnetization data in (a) are vertically offset for clear comparison.

4.2.6. Dependence of the multiferroic properties of NiY(1.5) by the initial components of the flux.

Figure 4.11 shows the temperature dependence of the in-plane magnetization of NiY(1.5) crystals with several different conditions. The black line indicates NiY(1.5) grown without the thermal process (TP) [used as crystals in above sections]. The red line indicates NiY(1.5) grown with the thermal process (TP) [used crystals in RcXRD]. The green line indicates NiY(1.5) grown by condition 1. The measurements were carried out at 0.01 T. Inverted triangles denote the transition point from the ferrimagnetic to screw magnetic ordered state for the respective crystals. As a result of growth by condition 1, the transition point from the ferrimagnetic to screw magnetic ordered state increases to ≈ 340 K, compared with that of the other NiY(1.5) grown by the same initial

components. This temperature is higher than that of ZnY(1.5) [≈ 320 K (see also Fig. 5.2)], MgY(0) [~195 K in ref. 70] and room temperature. As far as we know, this is the highest transition point in the hexaferrite helimagnets. In a memory device utilizing the spin-chiral domains, the high transition points will be indispensable. Figure 4.12 shows the magnetic-field dependence of (a) in-plane magnetization, (b) electric polarization at selected temperatures, and (c) magnetic phase diagram for the NiY(1.5) crystal by condition 1. The behavior of magnetic field dependence of the polarization and magnetization is basically similar to the NiY(1.5) grown without TP, although an another new intermediate phase, named intermediate III, appears above 150 K in addition to intermediate I and II, and the boundaries are shifted. The ferroelectric intermediate I phase is sustained up to ≈ 250 K. We did not succeed in observing the electric polarization at $T > 77$ K due to its leaky behavior. Therefore, whether the intermediate III shows the electric polarization is ambiguous. Considering the change of the magnetic phase diagram by the annealing effect, it is suggested that the slight change of the crystal structure in NiY(1.5) affects the magnetic structure drastically. One of the possible origins of the stabling screw phase and change of the diagram is the slight increment of the Fe/Ni ratio since the condition 1 is "Fe_2O_3-rich" composition, leading Fe/Ni ratio to increase slightly. By optimizing the flux compositions and annealing conditions, further improvement of the screw transition point and ferroelectric phase is expected.

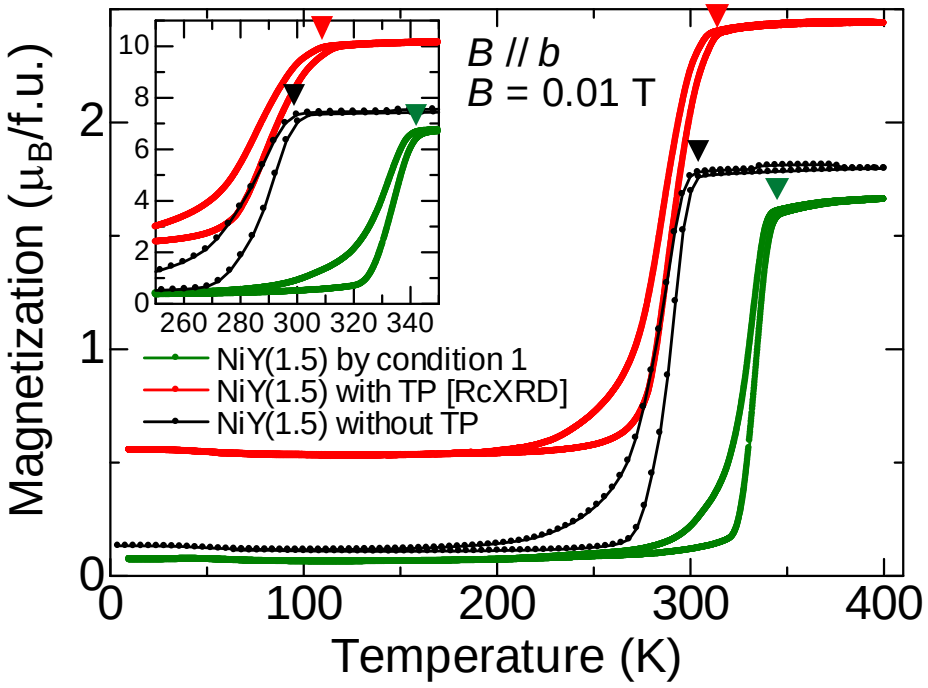

Figure 4.11 Temperature dependence of in-plane magnetization of NiY(1.5) crystals with several different conditions. The black line indicates NiY(1.5) grown without the thermal

process (TP) [used crystals in above sections]. The red line indicates NiY(1.5) grown with the thermal process (TP) [used crystals in RcXRD]. The green line indicates NiY(1.5) grown by condition 1. The measurements were carried out at 0.01 T. Inverted triangles denote the transition point from the ferrimagnetic to screw magnetic ordered state for the respective crystals.

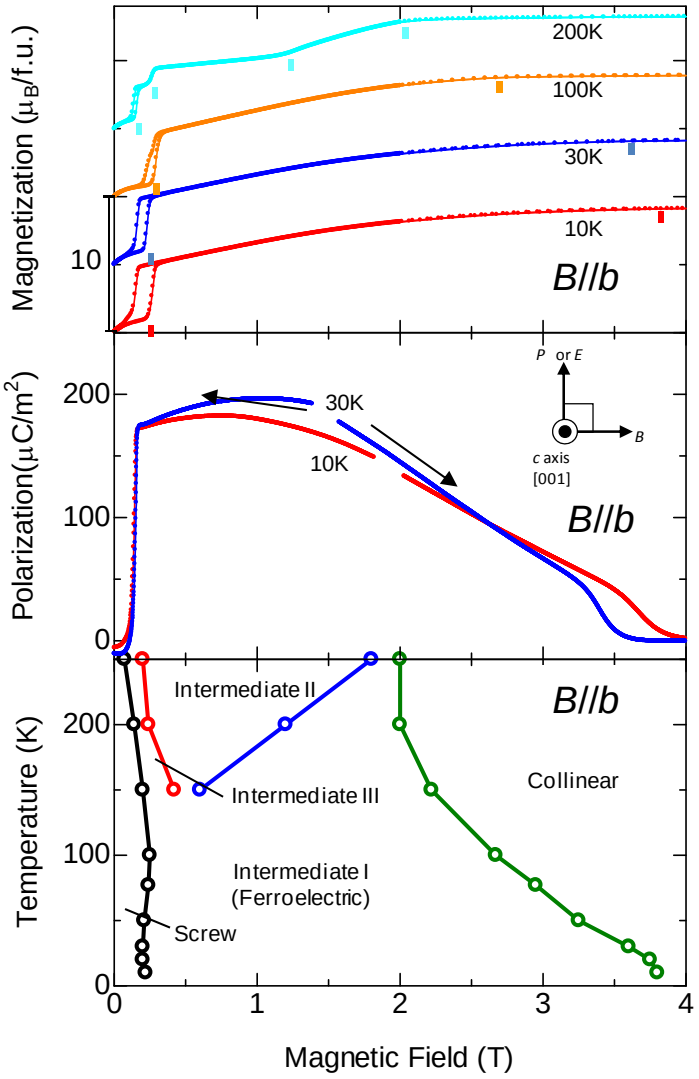

Figure 4.12 Magnetic-field dependence of (a) in-plane magnetization and (b) electric polarization at selected temperatures (c) Magnetic phase diagram for the NiY(1.5) crystal by condition 1.

4.3. Summary of this chapter

We investigated the magnetic and magnetoelectric properties of $Ba_{2-x}Sr_xNi_2Fe_{12}O_{22}$ ($0 \leq x \leq 1.5$)

single crystals with Y-type hexaferrite structure. In all the crystals, a ferrimagnetic order develops below ~660 K. For $x \leq 0.5$ crystals, the ferrimagnetic order remains down to the lowest temperature. For $x > 0.5$ crystals, in addition to the ferrimagnetic ordered states, a screw antiferromagnetic order develops at low temperature, i.e., the transition temperature from the ferrimagnetic to the antiferromagnetic ordered state.

The $x = 1.5$ crystal involves four magnetic ordered phases: the screw, intermediate I, intermediate II, and collinear phases, when external magnetic field B is applied perpendicular to the c axis. The intermediate I phase accompanies distinct electric polarization (2×10^2 $\mu C/m^2$ at 10 K). The ferroelectric intermediate I phase is sustained up to 250 K, however, we could not observe the electric polarization above 100 K due to its leaky behavior. By annealing the $x = 1.5$ crystal, an increase of resistivity by 10^3 times was observed at 300 K. Using the annealed crystal, we succeeded in observing the electric polarization up to ~175 K.

In addition, by changing the flux of the initial composition, stabilization of the screw below ~ 340 K is observed with the appearance of the new intermediate phase, named intermediate III.

Neutron diffraction measurements on an $x = 1.5$ crystal revealed that the screw phase is characterized by the incommensurate wave vector $k_{IC} = (0\ 0\ \delta)$, while both the intermediate I and II phases are characterized by the commensurate wave vectors $k_0 = (0\ 0\ 0)$ and $k_{3/2} = (0\ 0\ 3/2)$. The intensities of the magnetic reflections of the intermediate I and II phases are distinct from each other, which is probably attributable to the difference in the magnitude of the electric polarization between the two intermediate phases. However, more detailed experiments are needed to fully clarify the magnetic structures of these phases.

Chapter 5 Observation of spin-chiral domains in $Ba_{0.5}Sr_{1.5}Zn_2Fe_{12}O_{22}$ [ZnY(1.5)] and $Ba_{0.5}Sr_{1.5}Ni_2Fe_{12}O_{22}$ [NiY(1.5)] by scanning resonant X-ray microdiffraction

5.1. Introduction

The hexaferrites $Ba_{0.5}Sr_{1.5}Zn_2Fe_{12}O_{22}$ [ZnY(1.5)] and $Ba_{0.5}Sr_{1.5}Ni_2Fe_{12}O_{22}$ [NiY(1.5)] were found to show magnetic-field-induced ferroelectricity triggered by metamagnetic transitions. Their crystal structure with the centrosymmetric space group $R\bar{3}m$ ($a \approx 5.86$ Å and $c \approx 43.4$ Å) is composed of alternating stacks of S and L blocks along the c axis. In ZnY(1.5) and NiY(1.5), a proper screw magnetic structure with two chiral domains is illustrated in Figure 5.1 (b) and (c). It is worth noting that the proper screw spiral magnetic structure of the ZnY(1.5) is stabilized below $T_N \approx 320$ K though paramagnetism directly, whereas that of NiY(1.5) is stabilized below $T_c \approx 310$ K though a ferrimagnetic phase with a collinear magnetic structure [Figure 5.2].

In this chapter, we report the observation of spin-chiral domains on a clean cleaved surface of ZnY(1.5) and NiY(1.5) crystals by means of the scanning X-ray microdiffraction technique using a circularly polarized and highly focused X-ray beam.

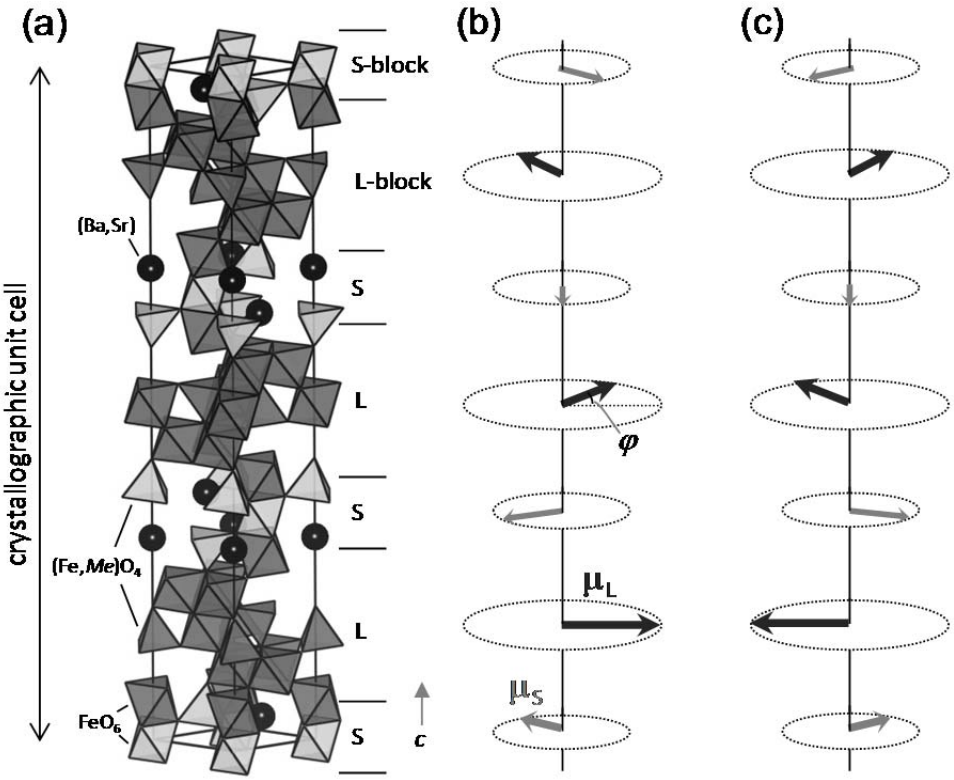

Figure 5.1 Crystallographic and helimagnetic structures of $Ba_{0.5}Sr_{1.5}Me_2Fe_{12}O_{22}$ (*Me* = Zn

or Ni) (a) Crystal structure composed of alternating stacks of S and L blocks. (b) and (c) Right- and left-handed spin-chiral structures, respectively.

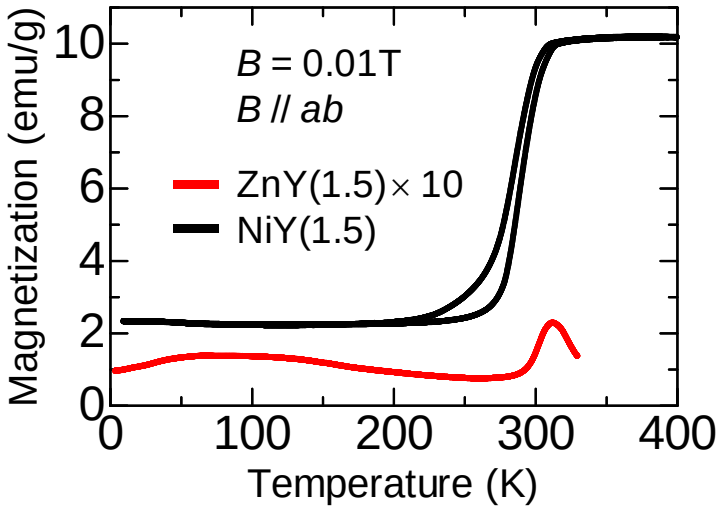

Figure 5.2 Temperature dependence of in-plane magnetization of the NiY(1.5) and ZnY(1.5) crystal. The measurements were carried out at 0.01 T.

5.2. Experimental results

5.2.1. The observation of Spin-chiral domains in ZnY(1.5)

Figure 5.3(a) shows (0 0 L) scans between the (0 0 2) and the (0 0 4) positions at 74 K on a certain sample position (Y = 0.5, Z = 0). The penetration depth ξ of the incident beam into the hexaferrite crystal was estimated from the full width at half maximum ΔQ of the (0 0 3) Bragg reflection. By using the relation, $\xi = 2\pi/\Delta Q$, where the unit of ΔQ is the reciprocal nanometer, we obtained $\xi \approx 40$ nm at the Fe L_3 edge.

Along with the (0 0 3) Bragg reflection, two magnetic satellite peaks are evident at (0 0 3±ε) with ε = 0.64. The sign change in the helicity of the circularly polarized incident x rays yields substantially different intensities of the magnetic reflections. The (0 0 3 − ε) reflection is more intense for incident x rays with the positive (+) helicity than with the negative (−) one, whereas (0 0 3+ε) by (+) helicity x rays is weaker than that by (−) ones. This result is essentially consistent with a previous resonant x-ray diffraction study[71]. However, the helicity-dependent magnitude relations of the (0 0 3±ε) intensities were reversed completely at another sample position (Y = 1.1, Z = 0), as displayed in Fig. 5.3 (b). For the data shown in Fig. 5.3 (a), the ratios of the (0 0 3 ± ε) intensities obtained by (−) helicity X-rays to those by (+) ones are I(003−ε) (−)/I(003−ε) (+) = 0.24 and I(003+ε) (−) /I(003+ε)(+) = 5.8. Meanwhile, $I_{(003-\varepsilon)}^{(-)}/I_{(003-\varepsilon)}^{(+)}$ = 4.8 and $I_{(003+\varepsilon)}^{(-)}/I_{(003+\varepsilon)}^{(+)}$ = 0.20 for the data of Fig. 5.3 (b). These results suggest that the spin chirality in these two positions are opposite in sign to each other. The resonant intensity of the magnetic satellites for the

helimagnetic structure of the hexaferrite has been formulated by Mulders *et al.*[71] using the second term of the equations (1-6).According to their calculation, the magnetic diffraction intensity along the *c* axis from right- and left-handed spin-chiral domains for circularly polarized X-rays are given by

$$I_{\text{right}} \propto \left(\cos^2\theta + \frac{1}{2}\sin^2\theta \mp \chi \cos\theta \sin 2\theta\right) \times [F_{11} - F_{1-1}]^2 \delta(\boldsymbol{q} - 3n\boldsymbol{G} \pm \varepsilon), \quad (5\text{-}1)$$

$$I_{\text{left}} \propto \left(\cos^2\theta + \frac{1}{2}\sin^2\theta \pm \chi \cos\theta \sin 2\theta\right) \times [F_{11} - F_{1-1}]^2 \delta(\boldsymbol{q} - 3n\boldsymbol{G} \pm \varepsilon), \quad (5\text{-}2)$$

where F_{11} and F_{1-1} are the atomic properties of the initial and excited states of the Fe ion, and $\boldsymbol{q}$ ($=\boldsymbol{k}_i - \boldsymbol{k}_f$), $\boldsymbol{G}$, $\boldsymbol{\varepsilon}$,and θ denote the wave vector transfer between incident and diffracted radiation, the reciprocal lattice vector, the magnetic propagation vector, and the Bragg angle, respectively. χ =+1 for the (+) helicity of the incident beam, whereas χ =−1 for the (−) helicity.

If the fractions of the right- and left-handed spin-chiral domains on the area irradiated by the x-ray beam are *a* and (1 − *a*), respectively, the diffracted intensity is given by

$$I_{\text{a}} \propto \left(\cos^2\theta + \frac{1}{2}\sin^2\theta \pm (1-2a)\chi \cos\theta \sin 2\theta\right) \times [F_{11} - F_{1-1}]^2 \delta(\boldsymbol{q} - 3n\boldsymbol{G} \pm \varepsilon), \quad (5\text{-}3)$$

Thus, the intensity ratio by the incident X-ray beam with the (−) helicity to that with the (+) helicity for the (0 0 3*n* ± *ε*) magnetic reflection can be written as

$$\frac{I_a^{(-)}}{I_a^{(+)}} = \frac{\cos^2\theta + \frac{1}{2}\sin^2\theta \mp (1-2a)\cos\theta \sin 2\theta}{\cos^2\theta + \frac{1}{2}\sin^2\theta \pm (1-2a)\cos\theta \sin 2\theta} \quad (5\text{-}4)$$

By applying Eq. (5-4) to the present experimental data, the population ratio between the right- and the left-handed spin chiral domains at a beam spot can be estimated. The results are summarized in Table 5.1 and demonstrate that the area measured for the data shown in Figs. 5.3(a) and 5.3(b) consists of nearly a mono domain with the right- and left-handed spin-chiral states, respectively. These results also confirm that the spatial resolution is small enough to isolate “a single chiral domain.”

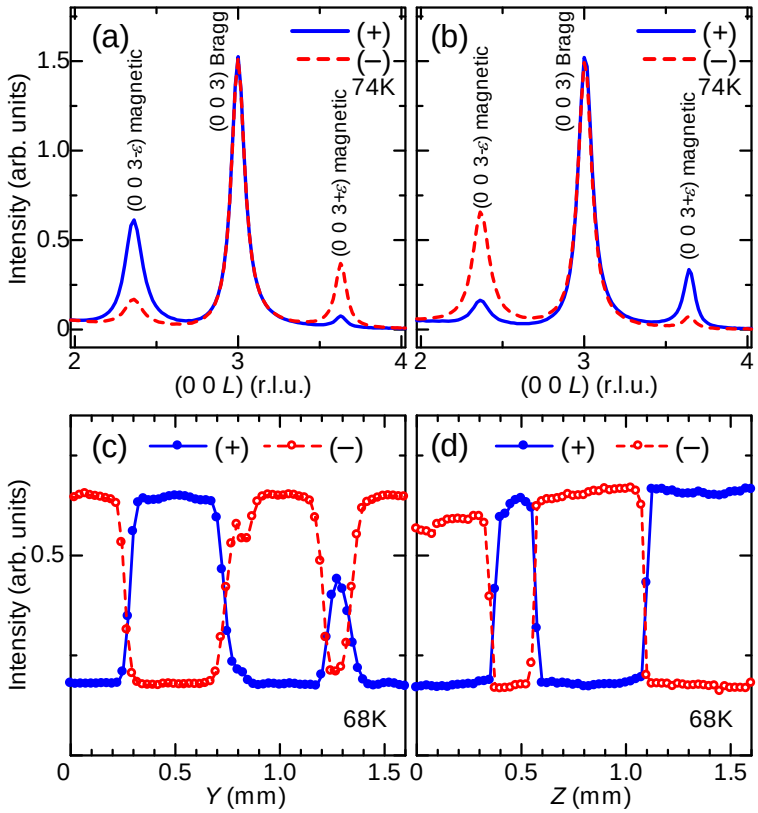

Figure 5.3 Sample position and circular X-ray polarization dependence of magetic reflection intensity. (a) and (b) X ray diffraction profiles of the (0 0 *L*) scan measured at different sample positions 0.6 mm distant. (c) and (d) X-ray peak intensities of the (0 0 3-*ε*) reflection as functions of horizontal (Y) and vertical (Z) sample positions, respectively. These measurements were carried out using (–)(broken red lines) and (+) (solid blue lines) helical incident X-rays with an energy corresponding the Fe L_3 edge.

	Fig. 5.3 (a) (at $Y = 0.5$, $Z = 0$)		Fig. 5.3 (b) (at $Y = 1.1$, $Z = 0$)	
Magnetic reflection	(0 0 3 – ε)	(0 0 3 + ε)	(0 0 3 – ε)	(0 0 3 + ε)
θ (degree)	28.4	47.0	28.4	47.0
$I^{(-)} / I^{(+)}$	0.24	5.8	4.8	0.20
a (fraction of right-handed domain)	97.2 %	100 %	0.2 %	2.8 %

Table 5.1 The observed intensity ratios of $I_{(0\,0\,3\pm\varepsilon)}^{(-)} / I_{(0\,0\,3\pm\varepsilon)}^{(+)}$, and the calculated fraction of the right-handed spin-chiral domains for the data shown in Figs. 5.3(a) and (b)

To further verify the sample position dependence of the spin chirality, we performed a microdiffraction scan in the Y and Z directions at the (0 0 3−ε) position with both (+) and (−) helical incident x rays. Figures 5.3(c) and 5.3(d) display the intensity profiles of the (0 0 3−ε) magnetic reflection as functions of the Y and Z positions, respectively, at 68 K. Two discrete levels

of the intensity alternately appear with a step width of 0.1 ~ 0.6 mm. More importantly, the intensity at each position is switched by changing the sign of the incident x-ray helicity, which means that the intensity profiles shown in Figs. 5.3(c) and 5.3(d) correspond to cross sections of spin-chiral domains. Thus, the present experimental setup of scanning resonant x-ray microdiffraction allows spin-chiral domains to be mapped by setting the sample to diffract on the magnetic satellite and scanning it through the X-ray beam.

Figure 5.4 shows a two-dimensional *YZ*-scanned intensity map of the (0 0 3−ε) magnetic reflection, i.e., a spin-chiral domain structure, over a 3 × 3 mm^2 area at 68 K. Red and blue correspond to high- and low-intensity counts, respectively. The images shown in Figs. 5.4 (a) and 5.4 (b) were taken from the same sample area by using (+) and (−) helical incident x rays, respectively. The color contrast is quite high and reversed from the image of Fig. 5.4 (a) to that of Fig. 5.4 (b). This confirms that the bright (red) and dark (blue) regions in the image of Fig. 5.4 (b) correspond to a left- and a right-handed spin-chiral monodomain, respectively, which covers almost all regions. The observed domains are irregular in shape, with a size on a submillimeter scale. The left- and right-handed spin-chiral domains are nearly equally populated. White boundaries, which are quite thin, correspond to the domain walls, which have no simple crystallographic orientations. By comparing the cross sections along the *Y* and *Z* axes shown in Figs. 5.3(c) and 5.3(d), we see that domain boundaries for the *Z* scan data are narrower than those for the *Y* scan data. This is because of better spatial resolution along the *Z* axis. The thickness is unknown at our resolution, but it is at least <50 μm, which is estimated by a deconvolution with the beam size. To our knowledge, the images shown in Fig. 5.4 have the highest contrast ever achieved for the magnetic chiral domains.

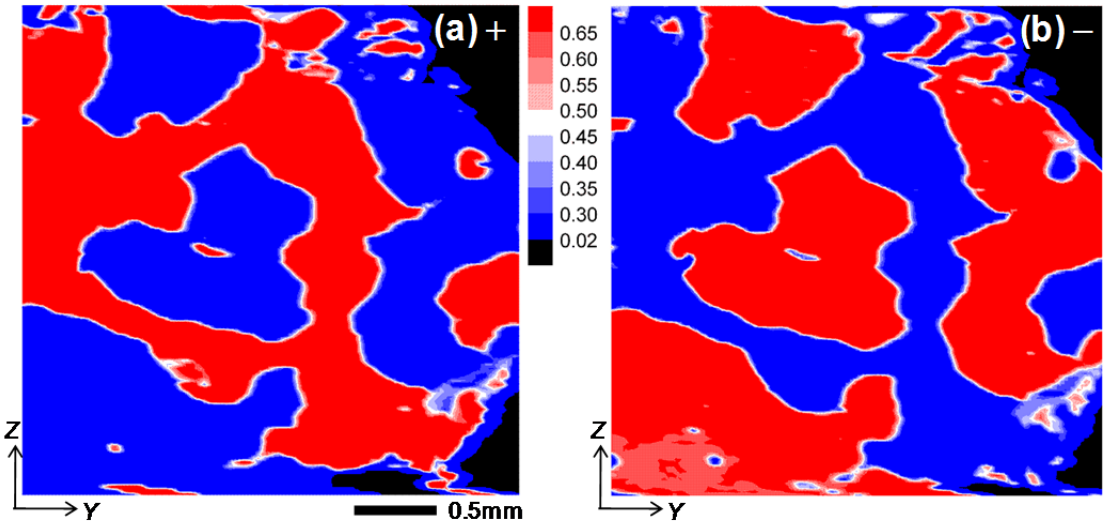

Figure 5.4 Spatial images of the spin-chiral domain structure in a single crystal of ZnY(1.5). (a) and (b) X-ray intensity maps of the (0 0 3−ε) magnetic reflection measured over a 3 × 3

mm^2 area at 68 K using (+) and (–) helical incident x-rays, respectively. Red and blue regions correspond to either a left- or right-handed spin-chiral domain. Black-colored areas represent off-sample regions.

Compared with spin-chiral domains observed in helimagnetic rare earth metals, the domain pattern (curved wall shape) and size (submillimeter scale) in the hexaferrite are somewhat similar to those in high-purity Tb and Ho single crystals after cooling from a paramagnetic phase. In the rare earth metals, the size of spin-chiral domains was found to be sensitive to the crystal purity (e.g., less than ~0.06 mm in an impure sample). We also performed scanning resonant X-ray microdiffraction measurements of another crystal of $Ba_{0.5}Sr_{1.5}Zn_2Fe_{12}O_{22}$ with a rougher surface.

Figure 5.5(a) displays a photograph of the surface. As seen in Fig. 5.5(a), the measured surface contains some defects such as dents, cracks, and steps. Figures 5.5(b) and 5.5(c) show two-dimensional intensity maps of the (0 0 3−ε) magnetic reflection at 75 K. Red and blue correspond to high- and low intensity counts, respectively. The images shown in Figs. 5.5(b) and 5.5(c) were taken at the same sample area by using (−) and (+) helical incident x rays, respectively. The color contrast is reversed from the image of Fig. 5.5(b) to that of Fig. 5.5(c), which confirms that red and dark blue regions correspond to either a left- or a right-handed spin-chiral domain. By closely comparing the surface photograph shown in Fig. 5.5(a) and the domain structures shown in Figs. 5.5(b) and 5.5(c), we find a tendency for the domain boundaries to be clamped at surface defects such as cracks, steps, and dents. In addition, the observed domains in the crystal were apparently smaller than those on a smooth surface (Compare Fig. 5.5 with Fig. 5.4.). The result appears to be similar to the case of the helimagnetic rare earth metals. To examine the evolution of the domain structure as a function of temperature, we measured two-dimensional intensity maps of the (0 0 3−ε) magnetic reflection at several temperatures for the crystal used in the measurements of Fig. 5.4. All measurements shown here were done using incident X-rays with (−) helicity. Before every mapping measurement, we checked the position of the (0 0 3−ε) magnetic reflection by measuring diffraction profiles along the reciprocal $c*$ axis at each temperature. The results are shown in Fig. 5.6 (a). Two sets of profiles are presented for the respective temperature data and correspond to the reflection from left- and right handed spiral domains. The (0 0 3−ε) magnetic reflection develops as temperature is decreased below T_N. The value of ε gradually decreases with decreasing temperature and is essentially consistent with that reported in a former neutron diffraction study. Before every mapping measurement, we oriented the crystal to diffract on the (0 0 3−ε) magnetic reflection at each temperature. Figures 5.6 (c)– 5.6 (e) show the observed intensity maps, i.e., spin chiral domains, at 273, 248, and 198 K, respectively. Figure 5.6 (b) displays a photograph of the crystal surface measured for this experiment. The measurements were done during the cooling process after the sample was heated to 330K ($>T_N$). Each figure has a different

scale of intensity. Although the contrast gradually becomes intense with decreasing temperature, the domain patterns at these three temperatures are qualitatively similar to one another. However, once the crystals are heated above T_N, the domain pattern changes. The intensity map shown in Fig. 5.6 (f) was taken for the same area at 47 K, but the crystal was again heated to 330 K($>T_N$) before the measurement. The domain structure shown in Fig. 5.6(f) is different from those shown in Figs. 5.6(c)– 5.6 (e). (In the absence of magnetic fields, there is no phase transition below T_N in the hexaferrite.) These results suggest that the domain structure is robust with respect to the variation of temperature and time once the spin-chiral domains are formed but is not reproducible once the crystal is heated above T_N.

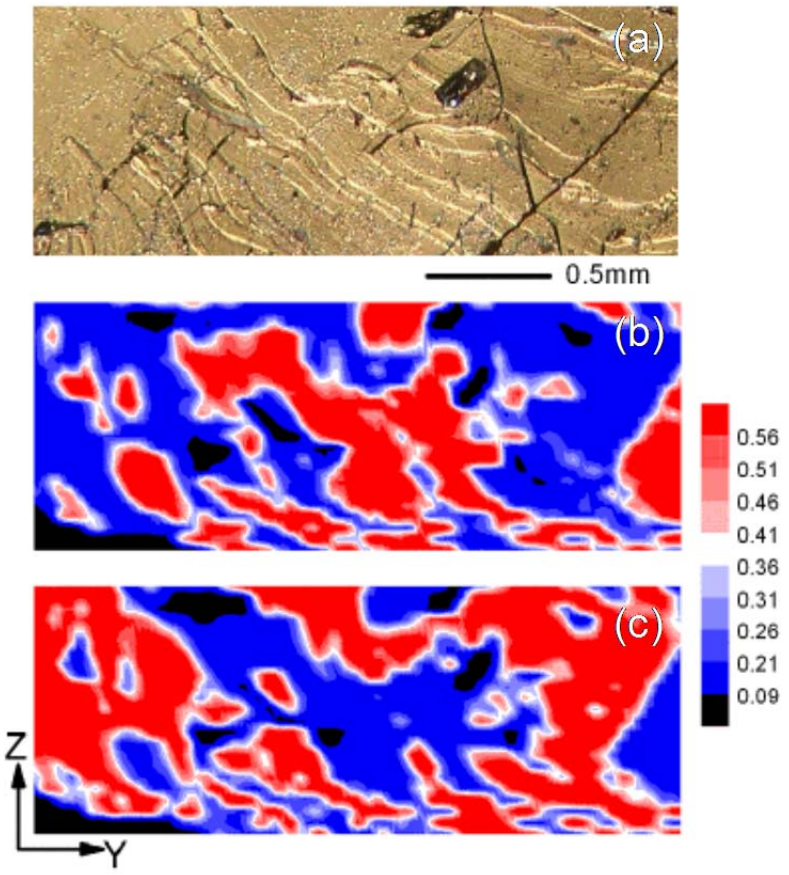

Figure 5.5 Spatial images of the spin-chiral domain structure in a crystal of ZnY(1.5) with a rough surface. (a) Photograph of the scanned surface of the crystal. (b) and (c) x-ray intensity maps of the (0 0 3–ε) magnetic reflection measured at 75 K using (–) and (+) helical incident X-rays, respectively. Red and blue regions correspond to either a left- or right- handed spin-chiral domain. Black areas represent regions with low intensities because of the roughness of the surface.

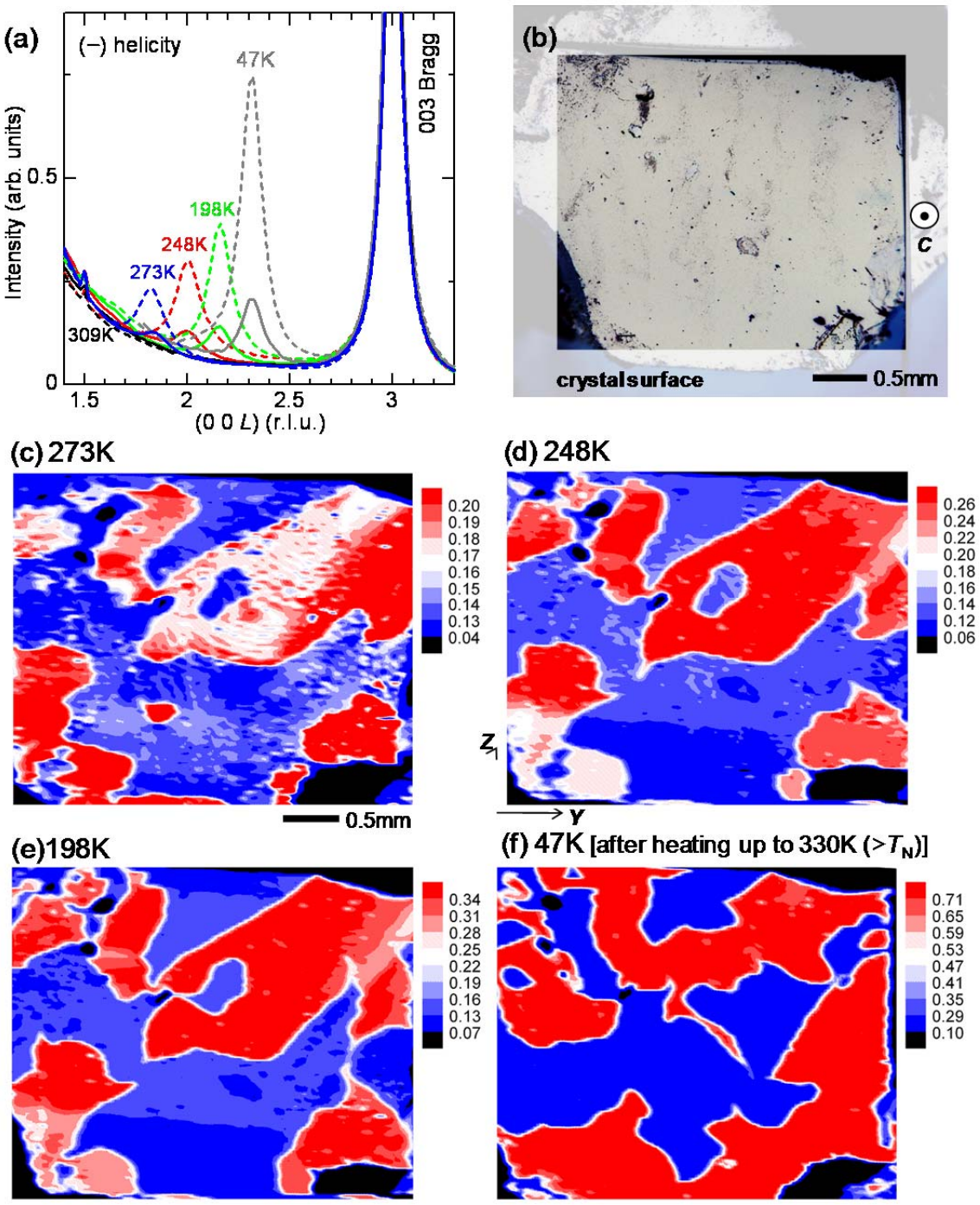

Figure 5.6 Temperature evolution of the spin-chiral domain structure in a single crystal of ZnY(1.5). (a) X-ray diffraction *L* scans along (0 0 *L*) at various temperatures. The small peak at L = 1.5 corresponds to the second harmonics of the (0 0 3) Bragg reflection. Broken and

solid lines represent the reflections from a left- and right- handed spin-chiral domain, respectively. (b) Photograph of the scanned surface of the crystal. (c)-(f) Spatial images of the spin-chiral domain structure at selected temperatures. These measurements were done using (–) helical incident X-ray at (c) 273 K, (d) 248 K, (e) 198 K and (f) 47 K. Before the measurement at (f) 47 K, the sample was heated to 330 K (> T_N).

5.2.2. Magneto-electric cooling effects on ZnY(1.5)

A proper screw magnetic structure, itself, does not induce the macroscopic electric polarization considering the spin current model, which makes the control of the spin-chirality difficult. By applying magnetic fields, however, it is expected that a cycloidal component whose spin-chirality can be controlled by an electric field appears. Siratori et al. reported that spin-chirality of a screw magnetic structure in $ZnCr_2Se_4$ can be controlled by a magneto-electric (ME) cooling, that is, cooling the sample from an ordered temperature with applying magnetic and electric fields, by means of a polarized neutron diffraction[72].

In this subsection, I will introduce the ME cooling effects on a ZnY(1.5). Experimental details are described in subsection 2.4.1. After the ME cooling, all the domain-scans are performed by using the (0 0 3−ε) magnetic reflection at 40 K and zero magnetic field.

Figure 5.7 (a) and (b) show spin-chiral domain structures in ZnY(1.5) after a ME cooling [+ E only] by (+) and (–) helicity, respectively. The spin-chiral domain structures after the ME cooling are similar to the above-mentioned ones without the ME cooling, and the cross sections of the spin-chiral domains show also same behavior[Fig 5.7 (c)], which reflects the fact that proper screw is electrically neutral.

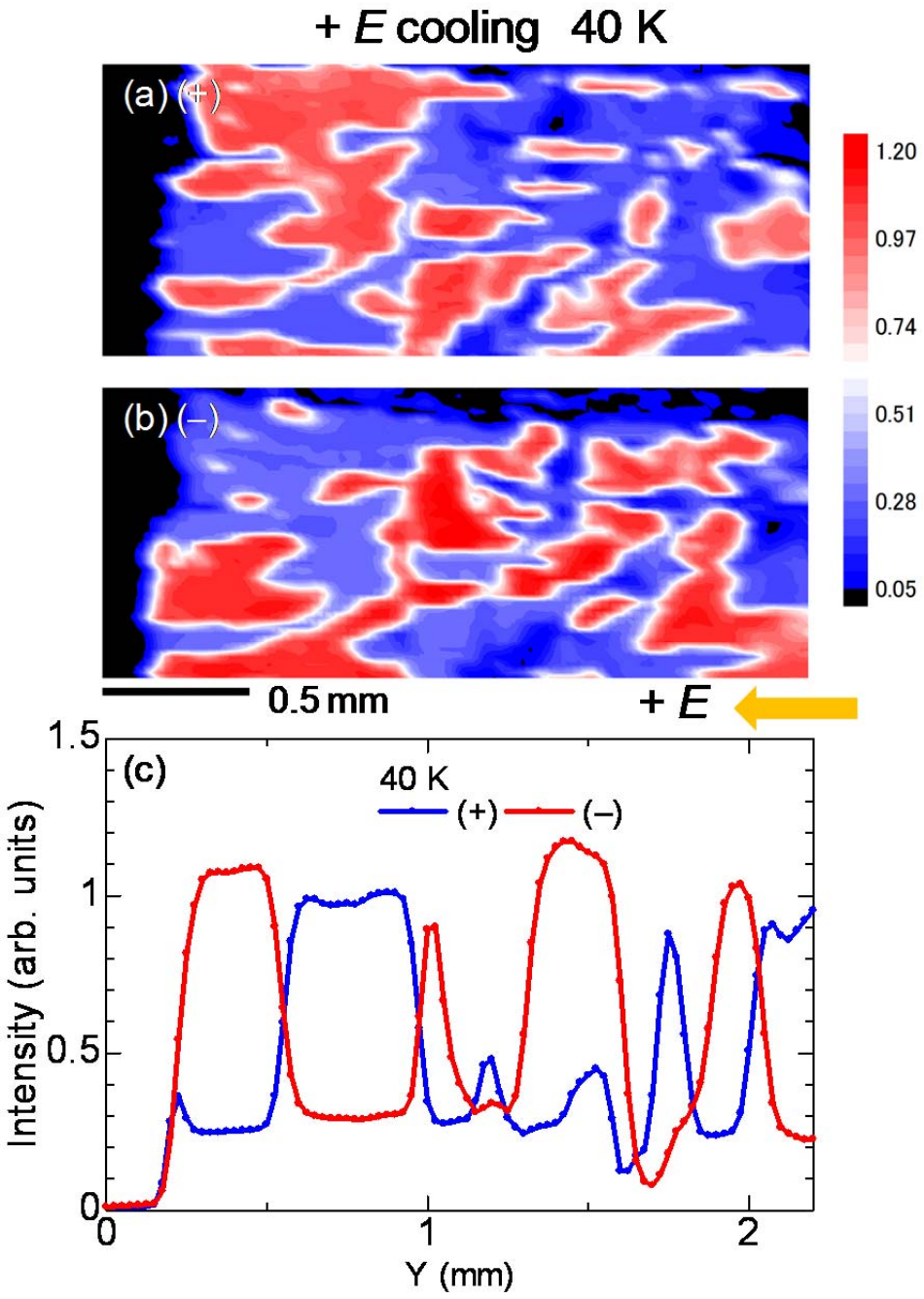

Figure 5.7 Spatial images of the spin-chiral domain structure in a single crystal of ZnY(1.5) after a ME cooling (only + *E*). (a) and (b) X-ray intensity maps of the (0 0 3−ε) magnetic reflection measured at 40 K using (+) and (–) helical incident X-rays, respectively. Black-colored areas represent off-sample regions. (c) X-ray peak intensities of the (0 0 3-ε) reflection as functions of horizontal (Y) sample position. This measurement was carried out using (+) (blue solid line) and (–) (red solid line) helical incident X-ray beam in a Z position.

Figures 5.8 (a) and (b) show spin-chiral domain structures after a ME cooling [+ E, − B] using (+) and (−) helicity, respectively. Nearly single spin-chiral domains by right-handed screw are observed

The intensities of the (0 0 3-ε) magnetic reflection at 40 K are not constant in a spin-chiral domain as shown by red and blue broken lines in Fig.5.8 (e), which suggests deformation of the proper screw as a result of the ME cooling because intensities of each spin-chiral domain from ideal proper screw should be constant, following eqs. (5-1) and (5-2). Asaka et al. reported that they consider the magnetic ground state of the ZnY(1.5) to be a distorted helical magnetic structure after 0.01T field cooling with the ferromagnetic component within the *ab* plane rather than the proper helical one by means of an electron diffraction technique [73]. When heating the sample to 200 K after the ME cooling [+ E, − B] with the electric and magnetic fields turning off, the position dependence in the spin-chiral domain became weakened. Figure 5.8 (f) shows magnetic field dependence of in-plane magnetization. The measurements are carried out with increasing magnetic field from 0 T to 0.04 T, (I) at 40 K after zero magnetic field cooling [ZFC]from 330 K to 40 K [a red solid line], (II) at 40 K after 0.1 T cooling from 330 K to 40 K [a black solid line], (III) at 200 K after ZFC from 330 K to 200 K [a red dashed line], and (IV) at 200 K after 0.1 T cooling from 330 K to 40 K, then, warming the sample from 40 K to 200 K at zero magnetic field [a black dashed line]. The *MB* curve in (II) increases rapidly around zero magnetic fields in contrast to that in (I), reflecting the ferromagnetic components within the *ab* plane,. This also indicate the magnetic field cooling causes the proper screw magnetic structure to be distorted with the ferromagnetic component even if the magnetic field is turned to zero.

However, when the sample is heated to 200 K without magnetic field after (II) process [corresponding to (IV)], its *MB* curve is close to those in (I) and (III), which indicate the deformation of the proper screw magnetic structure in 40 K can be removed by heating the sample at zero magnetic field to 200 K. Figures 5.8 (c) and (d) show spin-chiral domain structures using (+) and (−) helicity, respectively, when heating the sample from 40 K to 200 K without magnetic field after the measurements in Figs. 5.8 (a) and (b). Nearly single spin-chiral domains are kept but the patterns are modified somewhat, and the position dependence of the (0 0 3-ε) magnetic reflection in a spin-chiral domain is close to that in ideal proper screw [Fig. 5.3 (c-d) and 5.7 (c)] as shown by red and blue solid lines in Fig. 5.8(e).

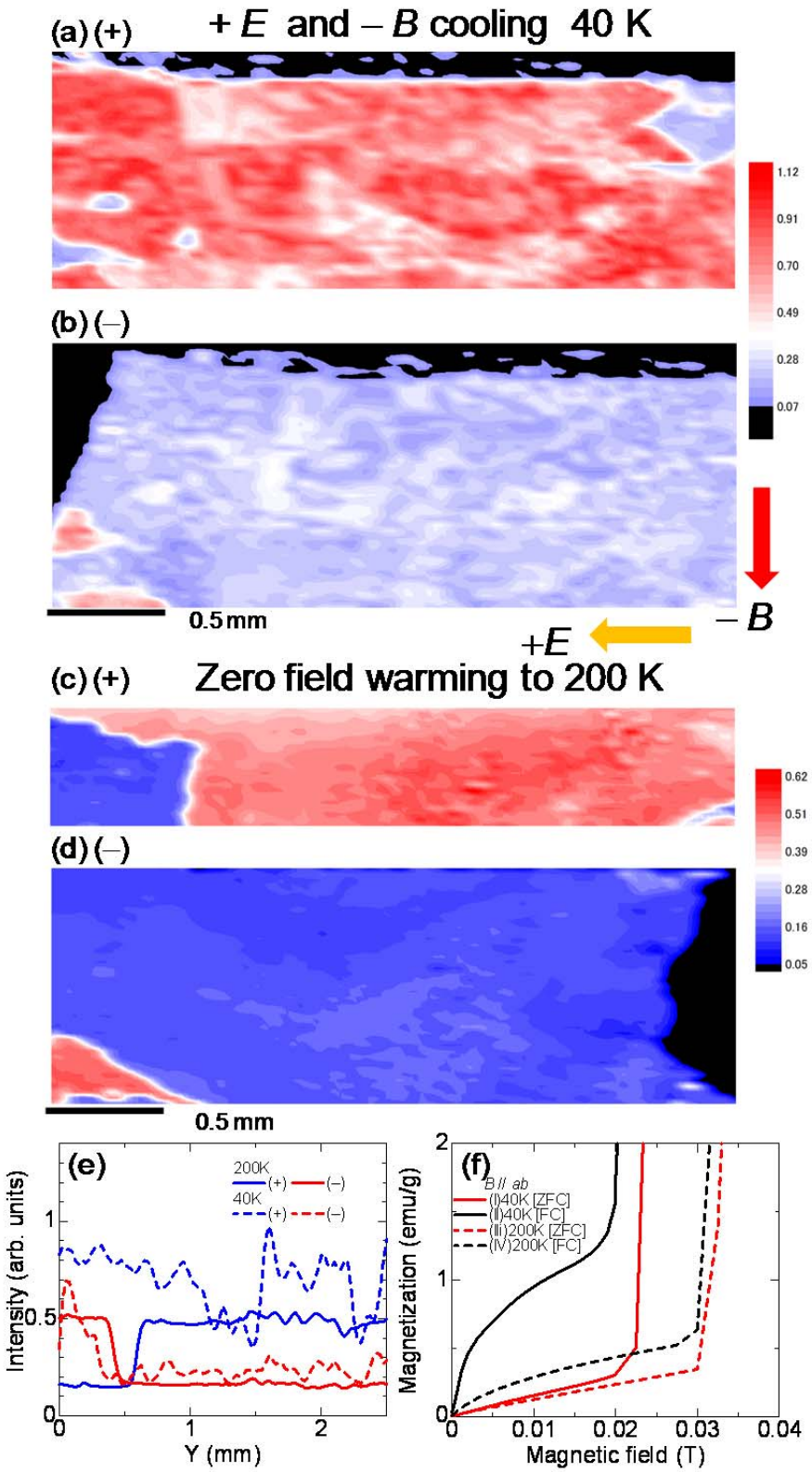

Figure 5.8 (a) and (b) show spin-chiral domain structures after a ME cooling [+ *E*, – *B*] using (+) and (–) helicity, respectively. (c) and (d) show spin-chiral domain structures using

(+) and (–) helicity, respectively, when heating the sample from 40 K to 200 K without magnetic field after the measurements in (a) and (b). (e) intensities of the (0 0 3-ε) reflection as functions of horizontal (Y) sample position. (+) [blue line] and (–) [red line] helical incident X-ray beam in a Z position in (a-b)[dashed lines] and (c-d) [solid line]. (f) shows magnetic field dependence of in-plane magnetization. The measurements are carried out with increasing magnetic field from 0 T to 0.04 T, (I) at 40 K after zero magnetic field cooling [ZFC]from 330 K to 40 K [a red solid line], (II) at 40 K after 0.1 T cooling from 330 K to 40 K [a black solid line], (III) at 200 K after ZFC from 330 K to 200 K [a red dashed line], and (IV) at 200 K after 0.1 T cooling from 330 K to 40 K, then, warming the sample from 40 K to 200 K at zero magnetic field [a black dashed line].

Figure. 5.9 shows two-dimensional domain scans after three different ME cooling conditions: [+ *E*, + *B*], [- *E*, + *B*], [+ *B* only] by (+) and (–) helicity beam. Although the polarity change of the electric field expects to lead to the change of the spin-chirality, Both the ME cooling [+ *E*, + *B*] and [- *E*, + *B*] cause nearly single chiral domain by the right –handed proper screw [Fig. 5.9 (a-d)]. It is noteworthy that even the ME cooling [+ *B* only] cause nearly single spin-chiral domains by left-handed. These results suggest that the magnetic field in the ME cooling affects formation of the nearly single spin-chiral domain patterns irrespective of whether applying an electric field or not.

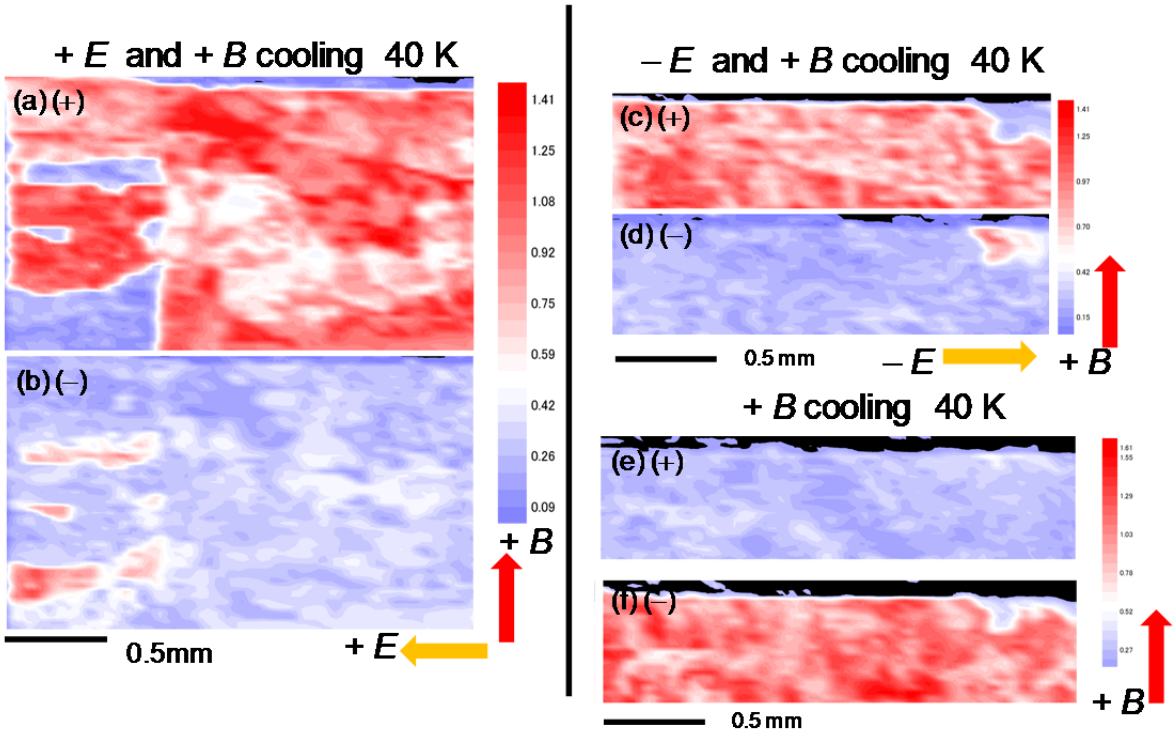

Figure 5.9 Spatial images of the spin-chiral domain structure in a single crystal of ZnY(1.5)

after a ME cooling [+ *E* and +*B*][(a) and (b)], [−*E* and +*B*] [(c) and (d)], and [only +*B*] [(e) and (f)] by means of X-ray intensity maps of the (0 0 3−ε) magnetic reflection measured at 40 K using (+) and (−) helical incident X-rays, respectively.

Discussion

Figure 5.10 shows phase diagram of ZnY(1.5) with *B* // *ab*. The magnetic field used for the ME cooling is estimated to 0.1 ~ 0.2 T. It cannot reach ferroelectric intermediate III but intermediate I or II. Momozawa et al. proposed the intermediate I and II are fanlike structures [Fig. 5. 10(b)], whose spin-charily cannot be defined, in the earlier studies by neutron diffraction[70]. This might be the reason why we could not control the spin-chirality by electric fields.

We observed the nearly single spin-chiral domains but, it remains unclear that these spin-chiral domains are derived from only surface or the whole bulk, because the penetration depth of the X-ray used in the experiments is ~40nm. Comparing the spin-chiral domain patterns in Figs. 5.8 (c-d) and Figs.5.9 (a-b) with the scanned ZnY(1.5) crystal in Fig.2.5 (b), sometimes the hair seam composes boundary of the spin-chiral domains. We speculate the length of the *c*-direction of the spin-chiral domains is thinner than depth of the hair seam, but further experiments are needed to verify the assumption.

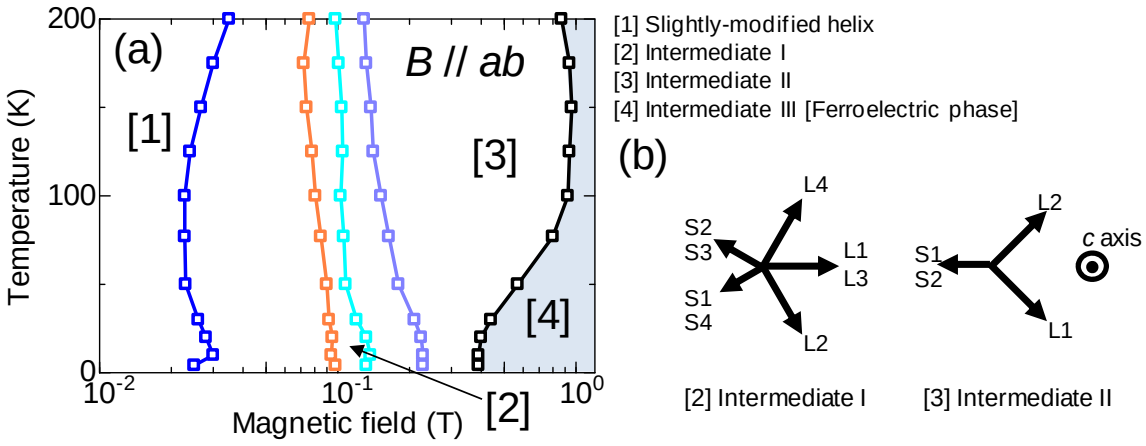

Figure 5.10 (a)Magnetic phase diagram for the ZnY(1.5) was determined by measurements of magnetization in the *B*-increasing runs with *B* // *ab*. (b) Proposed models in ref. 35 of intermediate I and II by applying *B* //*ab*.

5.2.3. The observation of spin-chiral domains in NiY(1.5)

Figure 5.11(a) shows X-ray diffraction L scans along (0 0 L) at various temperatures on the warming process. Black and white inverted triangles denote the (0 0 3 + ε) and (0 0 3 – ε) magnetic reflections, respectively. Black and white squares denote the (0 0 6 – 2ε) and (0 0 3 + 2ε) magnetic reflections, respectively. Solid and broken lines indicate (+) helicity and (–) helicity, respectively. Magnetic reflections are observed below 290 K, which reflects the transition point from the screw to collinear $T_c \approx 310$ K, as shown in Figure 5.2. The second harmonics are also observed, which is due to the $f_{\mathrm{lin}}(E)$ term in eqs (1-6), although I use only $f_{\mathrm{circ}}(E)$ for calculation for the diffracted intensities above.

In Figure 5.11(b), the temperature dependence of turn angle Φ_0 calculated from these reflections and neutron diffraction in Fig. 4.7 is shown. They are well consistent with each other. Fig. 5.11(c) displays a photograph of the crystal surface measured for this experiment. Fig. 5.11(d) and (e) x-ray display intensity maps of the (0 0 3 + ε) [ε = 0.88] magnetic reflection measured at 69 K using (+) and (–) helical incident X-rays, respectively. The region surrounded by white broken lines is a crystallographic domain slanted by ~ 0.3 ° from c axis. Due to the crystallographic domain, we could not obtain the diffracted intensity from the (0 0 3 + ε) magnetic reflection in this region. The spin-chiral domain structure of NiY(1.5) is close to that of ZnY(1.5).

As mentioned in section 5.1, the proper screw spiral magnetic structure of the ZnY(1.5) is stabilized below $T_N \approx 320$ K through paramagnetism directly, whereas that of NiY(1.5) is stabilized below $T_c \approx 310$ K through a ferrimagnetic phase with a collinear magnetic structure [Figure 5.2].

The transition in NiY(1.5) is first-order like, and *M*-*T* curve shows the hysteresis. We examined the ferri-screw transition at 290 K. Figure 5.12 shows (a) X-ray peak intensities of the (0 0 3) Bragg reflection as functions of horizontal (Y) sample positions by using (+) helicity. (b)X-ray diffraction profiles of the (0 0 *L*) scan measured at Y = 1.0 mm [green line in (a)] and Y = 1.25 mm [black line in (a)] at 290 K. The magnetic reflection by the collinear magnetic structure appears on the (0 0 3) Bragg reflection [see also subsection 4.2.4]. In Figure 5.12(a), a region where the intensity of the 0 0 3 Bragg is strong [colored by gray] and regions where the intensity of the (0 0 3) Bragg is weak are observed, which reflects the coexistence of collinear and screw magnetic structures. In (0 0 L) scan at a position [Y = 1.0 mm] in a region where the intensity of the 0 0 3 Bragg is strong, the magnetic reflections appear on the (0 0 3) Bragg, whereas in a position [Y = 1.25 mm] in regions where the intensity of the (0 0 3) Bragg is weak, the magnetic reflections appear on the (0 0 3±ε) reflections. I successfully observed the coexistence of collinear and screw magnetic structures of NiY(1.5) by using the (0 0 3) Bragg reflection.

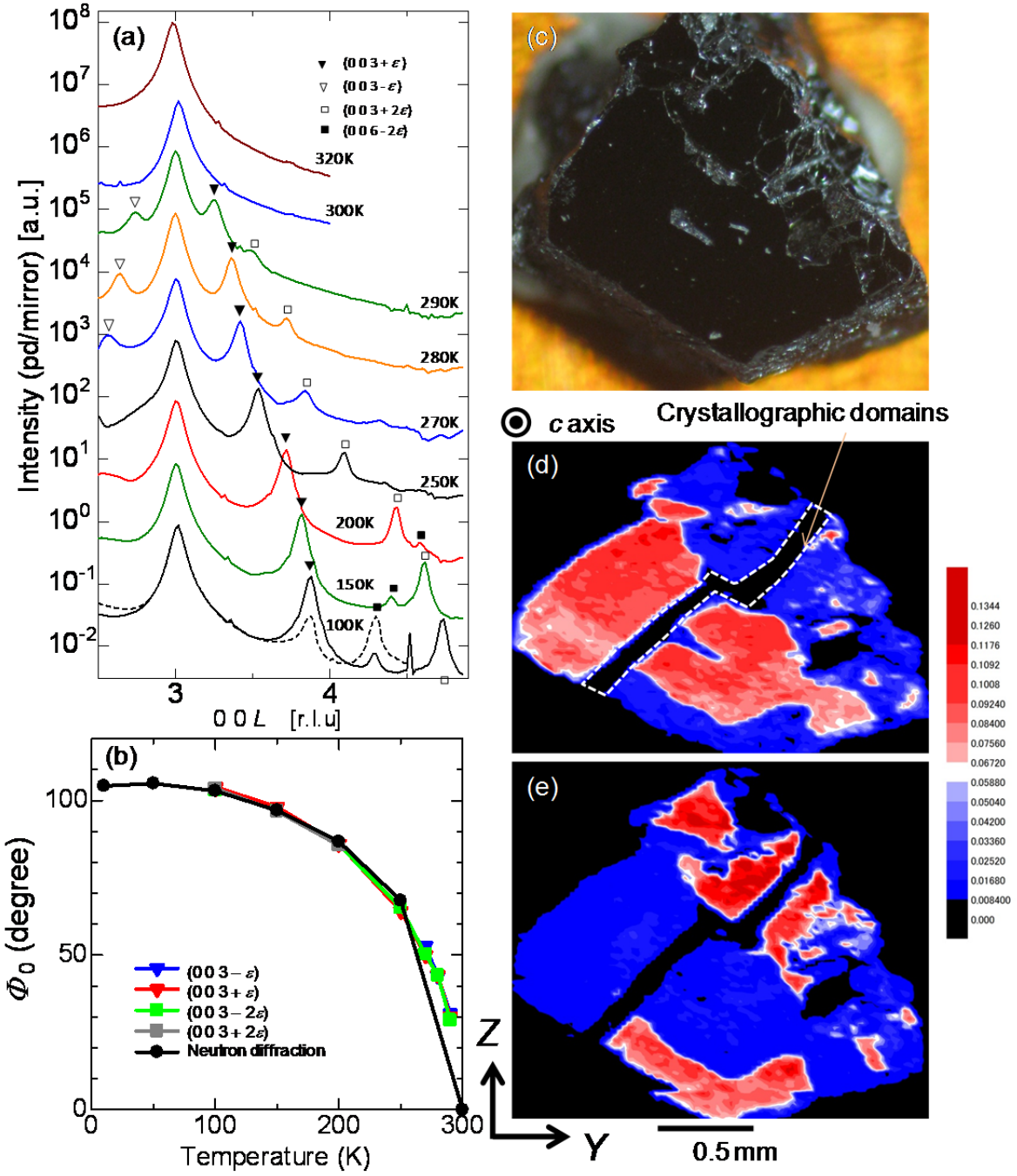

Figure 5.11 (a) X-ray diffraction *L* scans along (0 0 *L*) at various temperatures. Black and white inverted triangles denote the (0 0 3 + ε) and (0 0 3 – ε) magnetic reflections, respectively. Black and white squares denote the (0 0 6 – 2ε) and (0 0 3 + 2ε) magnetic reflections, respectively. Solid and broken line indicate (+) helicity and (–) helicity, respectively. [Intensities are represented by logarithmic scale] (b) Temperature dependence of turn angle Φ_0 calculated from the (0 0 3 + ε), (0 0 3 –ε), (0 0 6 – 2ε) and (0 0 3 + 2ε) reflections and Neutron diffraction in fig. 5.7. (c) Photograph of the scanned surface of the

crystal. (d) and (e) x-ray intensity maps of the (0 0 3 + ε) magnetic reflection measured at 69 K using (+) and (–) helical incident x-rays, respectively.

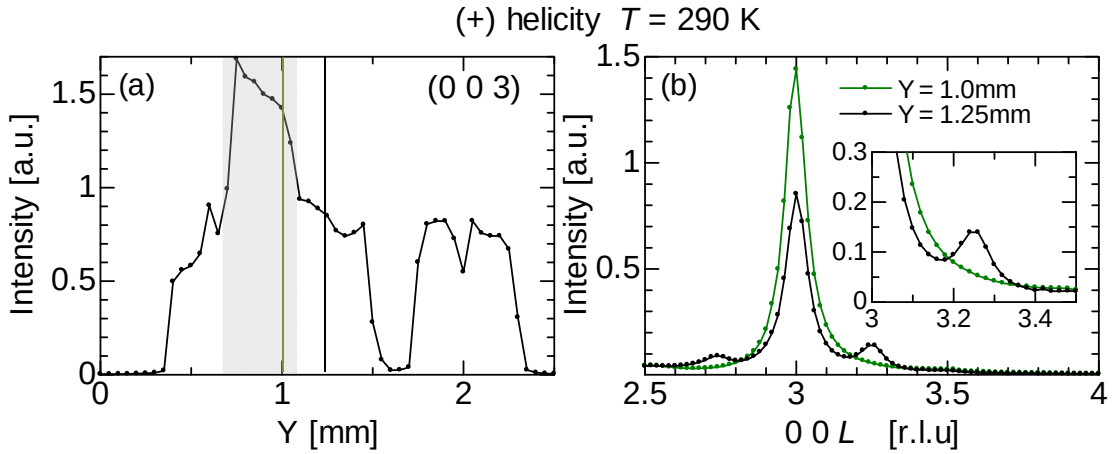

Figure 5.12 At 290 K, (a) X-ray peak intensities of the (0 0 3) Bragg reflection as functions of horizontal (Y) sample positions by using (+) helicity. (b)X-ray diffraction profiles of the (0 0 *L*) scan measured at Y = 1.0 mm [green line in (a)] and Y = 1.25 mm [black line in (a)].

5.3. Summary of this chapter

We investigated spatial maps of spin-chiral domains in helimagnetic $Ba_{0.5}Sr_{1.5}Zn_2Fe_{12}O_{22}$ [ZnY(1.5)] and $Ba_{0.5}Sr_{1.5}Ni_2Fe_{12}O_{22}$ [NiY(1.5)] by means of a scanning resonant x-ray microdiffraction technique using a circularly polarized and highly focused x-ray beam. This technique provides the necessary resolution and contrast to resolve self organizing spin-chiral domains on clean surfaces of helimagnets. We observed that domains are on a submillimeter-length scale and robust with respect to the variation of time and temperature once they form. We conducted also the ME cooling to ZnY(1.5), and realize the nearly single spin-chiral domains, although control of the spin-chiral domain by applying electric fields is unsuccessful.

In addition, coexistence of the collinear and screw magnetic structure is also observed near the transition point in NiY(1.5).

Chapter 6 Conclusion

Accomplishments obtained in this work

The main targets of this thesis are as follows:

(1) The discovery of new multiferroics in hexaferrites.

(2) Single crystal growth of multiferroic hexaferrites $(Ba,Sr)_3Co_2Fe_{24}O_{41}$.

(3) Imaging for "spin-chiral domains" by means of scanning resonant circularly polarized X-ray diffraction.

To achieve and reach these goals, we grew single crystals of hexaferrites by flux method as a first step. For (1-3), we performed macroscopic (magnetization, dielectric constant, and electric polarization) measurements. For (1), neutron diffraction measurements were performed to elucidate the origin of multiferroicity. In addition, to improve multiferroic properties, sample annealing and optimizing growth conditions also were performed. For (2), we optimized the flux of the initial components to grow the $(Ba,Sr)_3Co_2Fe_{24}O_{41}$ in Na_2O-Fe_2O_3 flux and BaO-B_2O_3 flux . For (3), we performed resonant circularly-polarized X-ray diffraction at SPring-8 BL17.

The obtained results though the measurements are:

[For purpose (1)]

We discovered that Y-type $Ba_{2-x}Sr_xNi_2Fe_{12}O_{22}$ ($0 \leq x \leq 1.5$) [NiY(x)] single crystals as new multiferroic materials, and investigated their magnetic and magnetoelectric properties. In all the crystals, a ferrimagnetic order develops below ~660 K. For $x \leq 0.5$ crystals, the ferrimagnetic order remains down to the lowest temperature. For $x > 0.5$ crystals, in addition to the ferrimagnetic ordered states, a screw antiferromagnetic order develops at low temperatures, i.e., the transition temperature from the ferrimagnetic to the antiferromagnetic ordered state.

The $x = 1.5$ crystal involves four magnetic ordered phases: the screw, intermediate I, intermediate II, and collinear phases, when external magnetic field B is applied perpendicular to the c axis. The intermediate I phase accompanies distinct electric polarization (2×10^2 $\mu C/m^2$ at 10 K). The ferroelectric intermediate I phase is sustained up to 250 K, however, we could not observe the electric polarization above 100 K due to its leaky behavior. By annealing the $x = 1.5$ crystal, an increase in resistivity of 10^3 times was observed at 300 K. Using the annealed crystal, we succeeded in observing the electric polarization up to ~175 K.

In addition, by changing the flux of the initial composition, stabilization of the screw below ~ 340 K is observed with the appearance of the new intermediate phase, named intermediate III,

Neutron diffraction measurements on an x = 1.5 crystal revealed that the screw phase is characterized by the incommensurate wave vector k_{IC} = (0 0 δ) while both the intermediate I and II phases are characterized by the commensurate wave vectors k_0 =(0 0 0) and $k_{3/2}$ = (0 0 3/2). The intensities of the magnetic reflections of the intermediate I and II phases are distinct from each other, which is probably attributable to the difference in the magnitude of the electric polarization between the two intermediate phases. However, more detailed experiments are needed to fully clarify the magnetic structures of these phases.

[For purpose (2)]

Unfortunately, competitors successfully grew $(Ba,Sr)_3Co_2Fe_{24}O_{41}$ [(Ba,Sr)CoZ] single crystals before I did. Following their findings, we tried to grow (Ba,Sr)CoZ single crystals by means of the Na2O-Fe2O3 flux, and optimized the flux condition to grow single crystals of (Ba,Sr)CoZ. (Ba,Sr)CoZ single crystals become stable in the (Ba,Sr) : Co = 1 :1 plane for Ba :Sr ratios of Sr-richer than Ba :Sr = 1 : 11.0798. we also obtained U-type $Sr_4Co_2Fe_{41}O_{60}$ [SrCoU] single crystals. This is the first report of the single crystal growth of the SrCoU, as far as I know.

In addition, by means of the $BaO-B_2O_3$ flux, I tried to grow BaCoZ which is difficult to grow in the Na2O-Fe2O3 flux. In the $BaO-B_2O_3$ flux, BaCoZ becomes stable and the region in the flux seems to be wide. This compensates for shortcomings of the $Na_2O-Fe_2O_3$ flux.

[For purpose (3)]

We investigated spatial maps of spin-chiral domains in helimagnetic $Ba_{0.5}Sr_{1.5}Zn_2Fe_{12}O_{22}$ [ZnY(1.5)] and $Ba_{0.5}Sr_{1.5}Ni_2Fe_{12}O_{22}$ [NiY(1.5)] by means of a scanning resonant x-ray microdiffraction technique using a circularly polarized and highly focused x-ray beam. This technique provides the necessary resolution and contrast to resolve self organizing spin-chiral domains on clean surfaces of helimagnets. We observed that domains are on a submillimeter-length scale and robust with respect to the variation of time and temperature once they form. We conducted also the ME cooling to ZnY(1.5), and realize the nearly single spin-chiral domains, although control of the spin-chiral domain by applying electric fields is unsuccessful. In addition, coexistence of the collinear and screw magnetic structure is also observed near the transition point in NiY(1.5).

Acknowledgments

This Ph.D. thesis could not have been completed without a number of people. My deepest gratitude goes to out to Prof. Tsuyoshi Kimura who always patiently helped me and generously supported all aspects of my life and study.

I would also like to thank Dr. Yoshikazu Tanaka of the RIKEN Harima Institute for experiments in SPring 8, fruitful discussions and allowing me to visit for two months.

Asso. Prof. Yusuke Wakabayashi and Asst. Prof. Hiroyuki Nakamura have helped me to develop a deeper understanding of my research process and mentored me well. I would like to express my appreciation to all the members of Kimura lab, especially to Mr. Takeshi Mochizuki for the crystal growth.

I am deeply grateful to Asso. Prof. Shigeki Miyasaka for a four-circle x-ray diffractometer, Asst. Prof. Tetsuya Takeuchi for SQUID, and Asst. Prof. Dr. Minoru Soda for neutron diffraction measurements and fruitful discussions.

I am also grateful to Ms. Etsuko Hazama, as an office administrator of Kimura lab, for her constant support and help.

Finally, I also would like to express my gratitude to my parents for supporting me financially and mentally.

Reference

[1] SW Cheong, MV Mostovoy, *Nature Mater.*, **6**,13 (2007)

[2] DI Khomskii, *Physics*, **2**, 20 (2009)

[3] T Kimura, T Goto, H Shintani, K,Ishizaka, T Arima, Y Tokura, *Nature*, **426**,55 (2003)

[4] Kitagawa, Yutaro, Yuji Hiraoka, Takashi Honda, Taishi Ishikura, Hiroyuki Nakamura, and Tsuyoshi Kimura, *Nature mater.,* **9**, 797–802 (2010)

[5] R Seshadri, NA Hill, *Chem. Mater.*,**13**, 2892 (2001)

[6] BB Van Aken, TTM Palstra, A Filippetti, NA Spaldin, *Nature Mater.*, **3**,164 (2004)

[7] DV Efremov, J van den Brink, DI Khomskii, *Nature Mater.*, **3**,853–56 (2004)

[8] Y Tokunaga, T Lottermoser, Y Lee, R Kumai, M Uchida, et al., *Nature Mater.,* **5**, 937(2006)

[9] N Ikeda, H Ohsumi, K Ohwada, K Ishii, T Inami, et al., *Nature,* **436**,1136 (2005)

[10] T Kimura., *Annu. Rev. Mater. Res.*, **37**, 387 (2007)

[11] Y. J. Choi et al., *Phys. Rev. Lett*., **100**, 047601 (2008)

[12] T. Arima, *J. Phys. Soc. Jpn.,* **76**, 073702 (2007)

[13] H. Katsura, N. Nagaosa, and A. V. Balatsky, *Phys. Rev. Lett.*, **95**, 057205 (2005)

[14] M. Mostovoy, *Phys. Rev. Lett.*, **96**, 067601, (2006)

[15] I. A. Sergienko and E. Dagotto, *Phys. Rev. B*, **73**, 094434, (2006)

[16] P. Curie, *J. phys. 3 (Ser. III)*, **37**, 40-54,(1984)

[17] T. H. O'Dell, "*The electrodynamics of Magneto-electric Media*" Amsterdam : North Holland (1970).

[18] A. J. Freeman and H.Schmid, eds., "*Magnetoelectric Interaction Phenomena in Crystals*" London: Gordon &Breach (1975).

[19] I. E. Dzyaloshinskii, *Sov. Phys. JETP*, **10**, 628-629 (1960)

[20] D.N. Astrov, *Sov. Phys. JETP*, **11**, 708 (1960)

[21] H. shumid, "*Magnetoelectric effects in insulatng magnetic mateials*", in "*introduction to complex mediums for optics and elctromagnetics*" eds. W. S. Weiglhoger and A. Lakhtakia (Bellingham, WA:SPIE Press) pp. 167-95 (2003)

[22] R.C. Pullar , *Progress in Materials Science*, **57**, 1191–1334, (2012)

[23] G. Aminoff, *Geol Foren Stockh Forh*,**47**, 283 (1925).

[24] V. Adelskold , *Arkiv Kemi Min Geol*,**12a**, 1 (1938).

[25] JJ Went, GW Rathenau, EW Gorter, GW Van Oosterhout., *Philos Technol. Rev.*, **13**, 194 (1952)

[26] HPJ Wijn, *Nature* **170**,707 (1952)

[27] PB Braun, *Nature*,**170**,708 (1952)

[28] J Smit, HPJ Wijn. "*Ferrites"* Eindhoven, The Netherlands : Phillips Tech. Libr (1959)

[29] M Sugimoto. In: Wohfarth EP, editor. "*Ferromagnetic materials*", vol. 3. Amsterdam: North-Holland Physics Publishing; pp. 392–440 (1980)

[30] T. Kimura, *Annu. Rev. Condens. Matter Phys.*, **3,** 93-110 (2012)

[31] J. A. Kohn, D. W. Eckart, Charles F. Cook, Jr., *Science*, **172**,519-525 (1971)

[32] E.W. Gorter, *Proceedings of the IEE - Part B: Radio and Electronic Engineering,* **104,** 255-260,

(1957)
[33] OP Aleshko-Ozhevskiĭ, RA Sizov, VP Cheparin, II Yamzin. *Zh. Eksp. Teor. Fiz.,* **55**,820-830(1968) [*Sov. Phys. JETP*, **28**,425-430 (1969)]
[34] RA Sizov, KN Zaĭtsev. *Zh. Eksp. Teor. Fiz.,* **66**, 368-373 (1974). [*Sov. Phys. JETP*, **39**,175-177(1974)
[35] N Momozawa, Y Yamaguchi, *J. Phys. Soc. Jpn.,* **62**,1292-1304 (1993)
[36] U. Enz, *J. Appl. Phys.,* **32**, 22S-26S (1961)
[37] V. A. Sizov, R. A. Sizov, I.I. Yamzin, *Zh. Eksp. Teor. Fiz.* **55**, 1186-1190 (1968)[*Soviet physics JETP,* **28**, 619-621(1969)]
[38] T Kimura, G Lawes, AP Ramirez, *Phys. Rev. Lett.,* **94**,137201 (2005)
[39] Y. Tokunaga, Y. Kaneko, D. Okuyama, S. Ishiwata, T. Arima, S. Wakimoto, K. Kakurai, Y. Taguchi, and Y. Tokura," *Phys. Rev. Lett.*, **105**, 257201 (2010)
[40] K. Okumura, T. Ishikura, M. Soda, T. Asaka, H. Nakamura, Y. Wakabayashi, and T. Kimura, *Appl. Phys. Lett.*, **98**, 212504 (2011)
[41] S. H. Chun, Y. S. Chai, Y. S. Oh, D. Jaiswal-Nagar, S. Y. Haam, I. Kim, B. Lee, D. H. Nam, K.-T. Ko, J.-H. Park, J.-H. Chung, and K. H. Kim, *Phys. Rev. Lett.*, **104**, 037204 (2010)
[42] Hun Chang, Hak Bong Lee, Young-Sang Song, Jae-Ho Chung, S. A. Kim, I. H. Oh, M. Reehuis, and J. Schefer, *Phys. Rev. B*, **85**, 064402 (2012)
[43] K. Taniguchi, N. Abe, S. Ohtani, H. Umetsu, and T. Arima, A*ppl. Phys. Expr.*, **1**, 031301(2008)
[44] S .Ishiwata, Y Taguchi, H Murakawa, Y Onose, Y Tokura, *Science,* **319**,1643-1646 (2008)
[45] S. Ishiwata, Y. Taguchi, Y. Tokunaga, H. Murakawa, Y. Onose, and Y. Tokura, *Phys. Rev. B*, **79**, 180408 (2009)
[46] Yuji Hiraoka, Hiroyuki Nakamura, Minoru Soda, Yusuke Wakabayashi, and Tsuyoshi Kimura, *J. Appl. Phys.***, 110**, 033920 (2011).
[47] Hak Bong Lee, Sae Hwan Chun, Kwang Woo Shin, Byung-Gu Jeon, Yi Sheng Chai, and Kee Hoon Kim, *Phys. Rev. B,* **86**, 094435 (2012)
[48] Fen Wang, Tao Zou, Li-Qin Yan, Yi Liu, and Young Sun, *Appl. Phys. Lett.,* **100**, 122901 (2012)
[49] D. R. Harshman, E. D. Isaacs, D. B. McWhan, D. Mills and C. Vettier, *Phys. Rev. Lett.*, **61**, 1241-1244 (1988)
[50] S. W. lovesey and S. P. Collins "*X-Ray Scattering and Absorption by Magnetic Materials*" New York, the United States, Oxford University Press Inc. (1996)
[51] S. B. Palmer, J. Baruchel, A. Drillat, C. Patterson, and D. Fort, *J. Magn. Magn. Mater.* **54–57,** 1626-1628 (1986)
[52] J. Baruchel, *Physica B,* **192**, 79 (1993)
[53] J.C. Lang, D. R. Lee, D. Haskel, and G. Srajer, *J. appl. phys.*, **95** 6537-6539 (2004)
[54] P. G. Evans and E. D. Isaacs, *J. Phys. D: Appl. Phys*. **39**, R245 (2006)
[55] R. O. Savage and A. Tauber, *Mat. Res. Bull.* , **2**, 469-478, (1967)
[56] Hartmut Hibst , *Angew. chem. Int. Ed. Engl*. **21**, 270-282 (1982)
[57] Robert O. Savage and Arthur tauber, *J. Amer. ceram. soc.,* **47**, 13-18(1964)

[58] R C, Linares, *J. Amer. Ceram. Soc.,* **45(7)**, 307–310 (1962.)

[59] A. Tauber, Samuel Dixon, Jr., and R. O. Savage, Jr., J. Appl. phys., **35**, 1008–1009 (1964)

[60] T. takeuchi et al., *Rev. sci. instrum.,* **80**, 023905 (2009)

[61] Chun, Sae Hwan, Yi Sheng Chai, Byung-Gu Jeon, Hyung Joon Kim, Yoon Seok Oh, Ingyu Kim, Hanbit Kim, Byeong Jo Jeon, So Young Haam, Ju-Young Park, Suk Ho Lee, Jae-Ho Chung, Jae-Hoon Park, and Kee Hoon Kim, *Phys. rev. lett,* **108**, 177201(2012)

[62] We used these small pieces of U type for structural analysis. The results are summarized in following a paper:
Takashi Honda, Yuji Hiraoka, Yusuke Wakabayashi, Tsuyoshi Kimura, *J. Phys. Soc. Jpn.*, **82**, 025003 (2013)

[63] Minoru Soda, *private communications*

[64] N. Momozawa and M. Mita, *J. Cryst. Growth* **83**, 403 (1987)

[65] Y. S. Chai, S. H. Chun, S. Y. Haam, Y. S. Oh, I. Kim, and K. Hoon Kim, *New Journal of Physics*, **11** , 073030 (2009)

[66] R. A. Sizov, Sov. *Phys. Sol. St*., **23**, 1092-1093(1981)

[67] V. J. Folen, G. T. Rado, and E. W. Stalder ,*Phys. Rev. Lett*. **6**, 607–608 (1961)

[68] H. Sagayama, K. Taniguchi, N. Abe, T. Arima, Y. Nishikawa, S. Yano, Y. Kousaka, J. Akimitsu, M. Matsuura, K. Hirota, *Phys. Rev. B* **80** 180419(R) (2009)

[69] S. Ishiwata, D. Okuyama, K. Kakurai, M. Nishi, Y. Taguchi, Y. Tokura, *Phys. Rev. B,* **81**, 174418 (2010)

[70] Nobuyuki Momozawa, Yasuo Yamaguchi and Masaru Mita, *J. Phys. Soc. Jpn.* **55**, 1350-1358 (1986)

[71] M. Mulders et al., *Phys. Rev. B***, 81**, 092405 (2010).

[72] Kiiti Siratori, Jun Akimitsu, Eiji Kita, and Masakazu Nishi, *J. Phys. Soc. Jpn.*, **48,** 1111-1114 (1980)

[73]T. Asaka, X. Yu, Y. Hiraoka, K. Kimoto, T. Hirayama, T. Kimura, and Y. Matsui, *Phys. Rev. B*, **83**, 130401 (2011)

List of Publications

Journal

[1] "Dielectric, magnetic, and lattice dynamics properties of Y-type hexaferrite $Ba_{0.5}Sr_{1.5}Zn_2Fe_{12}O_{22}$: Comparison of ceramics and single crystals"
S. Kamba, V. Goian, M. Savinov, E. Buixaderas, D. Nuzhnyy, M. Maryško, M. Kempa, V. Bovtun, J. Hlinka, K. Knížek, P. Vaněk, P. Novák, J. Buršík, Y. Hiraoka, T. Kimura, K. Kouřil, and H. Štěpánková, *Journal of Applied Physics*, **107**, 104109 (2010)

[2] "Low-field magnetoelectric effect at room temperature"
Yutaro Kitagawa, Yuji Hiraoka, Takashi Honda, Taishi Ishikura, Hiroyuki Nakamura & Tsuyoshi Kimura, *Nature Materials*, **9**, 797–802 (2010)

[3] "Lattice modulation induced by magnetic order in the magnetoelectric helimagnet $Ba_{0.5}Sr_{1.5}Zn_2Fe_{12}O_{22}$"
T. Asaka, X. Z. Yu, Y. Hiraoka, K. Kimoto, T. Hirayama, T. Kimura, and Y. Matsui, *Physical. Review B,* **83**, 130401(R) (2011)

[4] "Spin-chiral domains in $Ba_{0.5}Sr_{1.5}Zn_2Fe_{12}O_{22}$ observed by scanning resonant x-ray microdiffraction"
Y. Hiraoka, Y. Tanaka, T. Kojima, Y. Takata, M. Oura, Y. Senba, H. Ohashi, Y. Wakabayashi, S. Shin, and T. Kimura, *Physical Reveviw B*, **84**, 064418 (2011)

[5] "Magnetic and magnetoelectric properties of $Ba_{2-x}Sr_xNi_2Fe_{12}O_{22}$ single crystals with Y-type hexaferrite structure"
Yuji Hiraoka, Hiroyuki Nakamura, Minoru Soda, Yusuke Wakabayashi, and Tsuyoshi Kimura, *Journal of Applied. Physics*, **110**, 033920 (2011)

[6] "Refinement of Crystal Structure of a Magnetoelectric U-Type Hexaferrite $Sr_4Co_2Fe_{36}O_{60}$"
Takashi Honda, Yuji Hiraoka, Yusuke Wakabayashi, Tsuyoshi Kimura, *Journal of the Physical Society of Japan*, **82,** 025003 (2013)

Proceedings

[1] "Hyperfine interactions in magnetoelectric hexaferrite system"
K. Kouril, V. Chlan, H. Stepankova, P. Novak, K. Knizek, J. Hybler, T. Kimura, Y. Hiraoka, and J. Bursik, *Journal of Magnetism and Magnetic Materials*, (2009), doi:10.1016/j.jmmm.2009.03.011.

Patent

[1] 特願 2010-138467 「電気磁気効果材料及びその製造方法」
特許番号　JP2012001396-A
出願人 国立大学法人大阪大学
発明者　木村 剛, 北川 祐太朗, 平岡 裕治, 中村 浩之, 石倉 太志
出願年月日　平成 22 年 6 月 17 日